Monthly Notices
of the
ROYAL ASTRONOMICAL SOCIETY

Mon. Not. R. Astron. Soc. **409,** 1705–1718 (2010) doi:10.1111/j.1365-2966.2010.17416.x

Continuous-wave gravitational radiation from pulsar glitch recovery

M. F. Bennett,⋆ C. A. van Eysden and A. Melatos

School of Physics, University of Melbourne, Parkville, VIC 3010, Australia

Accepted 2010 July 23. Received 2010 July 5; in original form 2009 December 21

ABSTRACT

Non-axisymmetric, meridional circulation inside a neutron star, excited by a glitch and persisting throughout the post-glitch relaxation phase, emits gravitational radiation. Here, it is shown that the current quadrupole contributes more strongly to the gravitational wave signal than the mass quadrupole evaluated in previous work. We calculate the signal-to-noise ratio for a coherent search and conclude that a large glitch may be detectable by second-generation interferometers like the Laser Interferometer Gravitational-Wave Observatory. It is shown that the viscosity and compressibility of bulk nuclear matter, as well as the stratification length-scale and inclination angle of the star, can be inferred from a gravitational wave detection in principle.

Key words: dense matter – gravitational waves – hydrodynamics – stars: neutron – pulsars: general – stars: rotation.

Downloaded from https://academic.oup.com/mnras/article/409/4/1705/986372 by guest on 16 August 2022

1 INTRODUCTION

Rotation-powered radio pulsars are promising sources of high-frequency gravitational waves. Their spin frequencies often lie in the hectohertz 'sweet spot' of current detectors, e.g. the Laser Interferometer Gravitational-Wave Observatory (LIGO). The rotation of their crusts can be measured extremely precisely, enabling coherent searches which improve the signal-to-noise ratio by the square root of the number of wave cycles observed. Such coherent searches have already beaten electromagnetic spin-down limits on the quadrupole moment of the Crab (Abbott et al. 2008) and are close for other pulsars (Abbott et al. 2007a). There are two main obstacles to detection. (1) Dephasing occurs if the radio pulses are used to construct a gravitational wave phase model but the fluid interior rotates at a slightly different speed to the crust. (2) The quadrupoles predicted so far are relatively small in isolated pulsars without any ongoing accretion activity, e.g. unstable oscillations such as *r*-modes (Brink, Teukolsky & Wasserman 2004; Nayyar & Owen 2006; Bondarescu, Teukolsky & Wasserman 2007), precession (Jones & Andersson 2002), internal magnetic deformations (Bonazzola & Gourgoulhon 1996; Cutler 2002), quasiradial fluctuations (Sedrakian et al. 2003; Sidery, Passamonti & Andersson 2010) and hydrodynamic turbulence (Melatos & Peralta 2010). Accreting millisecond pulsars can reach larger quadrupoles through magnetically confined mountains (Melatos & Payne 2005; Payne & Melatos 2006; Vigelius & Melatos 2009) or thermal mountains (Ushomirsky, Cutler & Bildsten 2000; Haskell, Jones & Andersson 2006).

In this paper, we investigate another source of gravitational radiation from isolated pulsars, namely the radiation emitted during the recovery phase following a pulsar glitch (van Eysden & Melatos 2008). Glitches are small, abrupt jumps $\Delta\nu$ in the rotation frequency ν which range in fractional size from 10^{-11} to 10^{-4} across the pulsar population and over four decades in individual objects. Currently, out of $\sim$1800 known pulsars, 101 have been observed to glitch, with a total of 285 individual events (Melatos, Peralta & Wyithe 2008). Glitches occur randomly in all but two objects (PSR J0537−6910 and PSR J0835−4510), which spin up quasi-periodically (Melatos et al. 2008). Most pulsars which have glitched at all have only glitched once. Of the 35 per cent that have glitched multiple times, and with the exception of the quasi-periodic pair, the glitch sizes and waiting times are well fitted by power-law and Poissonian probability density functions, respectively (Melatos et al. 2008), consistent with an avalanche mechanism (Warszawski & Melatos 2008; Melatos & Warszawski 2009).

Most theories of pulsar glitches build on the vortex unpinning paradigm introduced by Anderson & Itoh (1975). Superfluid vortices pin to lattice sites or defects in the crust and are prevented from migrating outward as the crust spins down electromagnetically. At some stage, many vortices unpin catastrophically, transferring angular momentum to the crust. While it is unknown what triggers the collective unpinning, it is likely to excite a non-axisymmetric flow for two generic reasons. (1) Pinning causes the crust and superfluid to rotate differentially, inevitably driving non-axisymmetric meridional circulation and even turbulence, as observed in laboratory experiments (Munson & Menguturk 1975; Nakabayashi 1983; Junk & Egbers 2000) and numerical simulations (Peralta et al. 2005, 2006a,b; Melatos & Peralta 2007; Peralta et al. 2008; Peralta & Melatos 2009) of spherical Couette flow. (2) Avalanche trigger mechanisms, like self-organized criticality, which are favoured by the observed glitch statistics, intrinsically lead to an inhomogeneous and hence non-axisymmetric superfluid velocity field, with spatial fluctuations correlated on all scales, from the smallest to the largest (Jensen 1998; Melatos et al. 2008).

⋆E-mail: mfb@unimelb.edu.au

© 2010 The Authors. Journal compilation © 2010 RAS

The gravitational wave signal from a pulsar glitch separates into two parts. First, there is a burst corresponding to non-axisymmetric vortex unpinning and rearrangement during the spin-up event itself. To date, observations have failed to resolve the spin-up time-scale. In the Vela pulsar, which was monitored continuously for several years, it occurs over less than 40 s (McCulloch et al. 1990; Dodson, McCulloch & Lewis 2002). Second, there is a decaying continuous-wave signal during the quasi-exponential relaxation phase (lasting days to weeks) following the spin-up event (Shemar & Lyne 1996). The latter signal arises as viscous interactions between the crustal lattice and core superfluid erase the non-axisymmetry in the superfluid velocity field and restore the crust and core to corotation (or at least steady differential rotation). Sidery et al. (2010) constructed a two-fluid 'body-averaged' model of a glitch and calculated that the burst signal emitted during the spin-up event by coupling to quasi-radial oscillations is too weak to be detected. In this paper, we focus on the second part of the signal, which has the advantage of enduring for many rotation periods, enabling a coherent search with increased signal to noise.

Two techniques have been proposed to date to search for gravitational radiation emitted during the spin-up event and post-glitch relaxation. Clark et al. (2007) developed a Bayesian selection criterion for comparing f-mode ring-down to white noise. Hayama et al. (2008) investigated coherent network analysis, which does not assume any particular waveform. Both methods would be aided by the availability of a specific signal template, like the one calculated in this paper. Importantly, by combining such a template with data, gravitational wave experiments can constrain the equation of state of bulk nuclear matter, complementing particle accelerator experiments which have recently produced results that disagree with astrophysical data. Heavy ion and nuclear resonance experiments measuring the compressibility of nuclear matter imply a soft equation of state (Sturm et al. 2001; Vretenar, Nikšić & Ring 2003), whereas neutron star observations imply a hard equation of state, albeit at lower energies (Hartnack, Oeschler & Aichelin 2006; Lattimer & Prakash 2007). Likewise, heavy-ion colliders measure a viscosity close to the conjectured quantum lower bound (Adare et al. 2007), whereas the relaxation time-scale of pulsar glitches suggests a value many orders of magnitude larger (Cutler & Lindblom 1987; Andersson, Comer & Glampedakis 2005; van Eysden & Melatos 2010). Gravitational wave observations will help to resolve these and other issues; bulk matter at nuclear density cannot be assembled in terrestrial laboratories with current technology (van Eysden & Melatos 2008; Owen 2009; Xu et al. 2009).

In this paper, we calculate the gravitational radiation generated from the spin up of the stellar interior following a pulsar glitch. We estimate its detectability with the current generation of long-baseline interferometers, and show that certain important constitutive properties of a neutron star can be extracted from gravitational wave data, at least in principle. The calculation is based on van Eysden & Melatos (2008), extended to treat current quadrupole radiation. In Section 2, we solve the general hydrodynamic problem of non-axisymmetric, stratified, compressible spin-up flow in a cylinder, driven by Ekman pumping, following an abrupt increase in the angular velocity of the container. The initial and boundary conditions implemented by van Eysden & Melatos (2008) are modified slightly to make them more realistic. In Section 3 we predict the gravitational radiation emitted during the relaxation phase following a glitch. We calculate the signal-to-noise ratio and estimate the detectability of the signal in Section 4. In Section 5, we show how to extract the compressibility, stratification and viscosity of the stellar interior from gravitational wave data.

2 EKMAN FLOW FOLLOWING A GLITCH

Radio pulse timing experiments have so far failed to resolve temporally the abrupt increase in the angular velocity of the neutron star crust during a glitch (McCulloch et al. 1990; Dodson et al. 2002). Hence, in the absence of more detailed information, we model a glitch as a step increase in the angular velocity Ω of a rotating, rigid, cylindrical container filled with a Newtonian fluid (Abney & Epstein 1996; van Eysden & Melatos 2008). A cylinder is a coarse approximation to a spherical star, but it admits analytic solutions and has a long history of being used to model neutron stars and in geomechanical studies (Pedlosky 1967; Walin 1969; Abney & Epstein 1996; van Eysden & Melatos 2008).

Differential rotation between the container and interior fluid drives Ekman pumping, which spins up the interior over time; see Benton & Clark (1974) for a review of Ekman pumping. The spin up of an axisymmetric container was first treated analytically by Greenspan & Howard (1963). For an incompressible fluid, the entire volume is spun up on the Ekman time-scale, $t_E = E^{-1/2}\Omega^{-1}$, where $E = \nu/(\Omega\, L^2)$ defines the dimensionless Ekman number in terms of the kinematic viscosity ν and the size L of the container. Subsequently, it was shown that compressibility and stratification reduce the spun-up volume by hindering flow along the side walls (Walin 1969; Abney & Epstein 1996; van Eysden & Melatos 2008). With less volume to spin up, the Ekman time-scale is lower. Non-axisymmetric spin up was analysed by van Eysden & Melatos (2008).

In this section, we solve the problem of the non-axisymmetric, stratified, compressible spin up of a cylinder, extending van Eysden & Melatos (2008). We write down the linearized hydrodynamic equations in Section 2.1, solve for the general spin-up flow in Section 2.2, apply initial and boundary conditions in Sections 2.3 and 2.4 and discuss precisely how and why these conditions differ from previous analyses. The final, time-dependent solutions for the pressure, density and velocity fields are presented in Section 2.5. We discuss the initial conditions for a glitch in Section 2.6. For full details of the calculation, the reader is referred to section 2 of van Eysden & Melatos (2008).

2.1 Model equations

Consider a cylinder of height $2L$ and radius L, containing a compressible, Newtonian fluid with uniform kinematic viscosity ν, and rotating about the z axis with angular velocity $\boldsymbol{\Omega} = \Omega \boldsymbol{e}_z$. In the rotating frame, the compressible Navier–Stokes equation reads

$$\frac{\partial \boldsymbol{v}}{\partial t} + \boldsymbol{v}\cdot\nabla\boldsymbol{v} + 2\boldsymbol{\Omega}\times\boldsymbol{v} = -\frac{1}{\rho}\nabla p + \boldsymbol{g} + \nu\nabla^2\boldsymbol{v} + \frac{\nu}{3}\nabla(\nabla\cdot\boldsymbol{v}) + \nabla\left(\frac{1}{2}\Omega^2 r^2\right). \quad (1)$$

The fluid satisfies the continuity equation

$$\frac{\partial \rho}{\partial t} + \nabla\cdot(\rho\boldsymbol{v}) = 0, \quad (2)$$

and the energy equation is written in a form that relates the convective derivatives of the pressure and density,

$$\left(\frac{\partial}{\partial t} + \boldsymbol{v}\cdot\nabla\right)\rho = \frac{1}{c^2}\left(\frac{\partial}{\partial t} + \boldsymbol{v}\cdot\nabla\right)p. \quad (3)$$

Downloaded from https://academic.oup.com/mnras/article/409/4/1705/986372 by guest on 16 August 2022

The symbols $\boldsymbol{v}$, ρ, p, $\boldsymbol{g}$ and c represent the fluid velocity, density, pressure, gravitational acceleration and the speed of sound, which is determined by the equation of state. Following Abney & Epstein (1996), gravity is taken to be uniform and directed towards the mid-plane of the cylinder,

$$\boldsymbol{g} = \begin{cases} -g\boldsymbol{e}_z & \text{if} \quad z > 0, \\ +g\boldsymbol{e}_z & \text{if} \quad z < 0, \end{cases} \tag{4}$$

where g is constant.

We work in cylindrical coordinates (r, ϕ, z) and consider the region $z \geq 0$, as the flow is symmetric about $z = 0$. Equations (1)–(3) are rewritten in dimensionless form by making the substitutions $t \mapsto t_E t$, $r \mapsto Lr$, $z \mapsto Lz$, $\boldsymbol{v} \mapsto L\,\delta\Omega\boldsymbol{v}$, $\rho \mapsto \rho_0\rho$, $p \mapsto \rho_0 gLp$ and $\nabla \mapsto (1/L)\nabla$, where the scalefactor ρ_0 is chosen to be the equilibrium density at $z = 0$. The scaled equations obtained in this way [see equations (6)–(8) in van Eysden & Melatos (2008)] feature three dimensionless quantities: the Rossby number $\epsilon = \delta\Omega/\Omega$, the Froude number $F = L\Omega^2/g$ and the scaled compressibility $K = gL/c^2$.

2.2 Spin-up flow

At time $t = 0$, the angular velocity of the cylinder accelerates instantaneously from Ω to $\Omega + \delta\Omega$. If ϵ is small, as in a pulsar glitch, the problem linearizes and we can solve for the equilibrium and spin-up flows separately by making the perturbation expansions $\rho \mapsto \rho + \epsilon\delta\rho$, $p \mapsto p + \epsilon\delta p$, and $\boldsymbol{v} \mapsto \boldsymbol{\delta v}$. In the frame rotating at Ω, the equilibrium velocity is zero and the spin-up flow is of order ϵ.

We assume that the equilibrium state is steady and axisymmetric, with $\rho = \rho(r, z)$ and $p = p(r, z)$. Ignoring centrifugal terms proportional to F, and taking $\rho^{-1}d\rho/dz$ to be uniform for simplicity, as in previous work (Walin 1969; Abney & Epstein 1996; van Eysden & Melatos 2008), we find

$$\rho(z) = \mathrm{e}^{-K_s z}, \tag{5}$$

$$p(z) = K_s^{-1}\mathrm{e}^{-K_s z}, \tag{6}$$

where $K_s = L/z_s = -L\rho^{-1}d\rho/dz$ is a constant which depends on the stratification length-scale, z_s.

The spin-up flow is unsteady and non-axisymmetric, with $\delta\rho = \delta\rho(r, \phi, z, t)$, $\delta p = \delta p(r, \phi, z, t)$, and $\boldsymbol{\delta v} = \boldsymbol{\delta v}\ (r, \phi, z, t)$. We solve equations (17)–(21) in van Eysden & Melatos (2008) for the spin-up flow using the method of multiple scales, expanding $\boldsymbol{\delta v}$, δp and $\delta\rho$ as perturbation series in the small parameter $E^{1/2}$, e.g. $\delta\rho = \delta\rho^0 + E^{1/2}\delta\rho^1 + O(E)$ (Walin 1969; Abney & Epstein 1996; van Eysden & Melatos 2008). Following section 2.3 in van Eysden & Melatos (2008), the $O(E^0)$ continuity equation is automatically satisfied and the order $O(E^{1/2})$ equations reduce to

$$\frac{1}{r}\frac{\partial}{\partial r}\left(r\frac{\partial\Phi}{\partial r}\right) + \frac{1}{r^2}\frac{\partial^2\Phi}{\partial\phi^2} - \frac{4K_s}{N^2}\frac{\partial\Phi}{\partial z} + \frac{4}{N^2}\frac{\partial^2\Phi}{\partial z^2} = 0, \tag{7}$$

where $N^2 = (K_s - K)/F$ is the dimensionless Brunt–Väisälä frequency and we define $\Phi = -\partial(\delta p^0/\rho)/\partial t$.

Equation (7) can be solved by separation of variables. The general solution that is regular as $r \to 0$ has the form

$$\Phi(r, \phi, z, t) = F\sum_{m=0}^{\infty} J_m(\lambda r)\left[A_m\cos(m\phi) + B_m\sin(m\phi)\right] \times Z_m(z)T_m(t), \tag{8}$$

where $m \geq 0$ is an integer and λ is determined by the boundary conditions. The prefactor F is included as Φ is expected to be of this order. This is the same result found by van Eysden & Melatos (2008) but is slightly more general than the equivalent in Abney & Epstein (1996), as it allows for the possibility that FN^2 and K are of similar magnitude, a likely scenario in a neutron star (van Eysden & Melatos 2008).

2.3 Boundary conditions

The boundary conditions on Φ are set by the boundary conditions on the $O(E^0)$ velocity fields,

$$\delta v_r^0 = -\frac{1}{2Fr}\frac{\partial}{\partial\phi}\left(\frac{\delta p^0}{\rho}\right), \tag{9}$$

$$\delta v_\phi^0 = \frac{1}{2F}\frac{\partial}{\partial r}\left(\frac{\delta p^0}{\rho}\right), \tag{10}$$

as Φ is defined in terms of δp^0 and is therefore $O(E^0)$ too. [To impose boundary conditions on the $O(E^{1/2})$ flow, we would need to know δp^1.] Assuming no penetration at the side wall, we have $\partial\Phi/\partial\phi = 0$ at $r = 1$ and hence

$$\Phi(r, \phi, z, t) = F\sum_{m=0}^{\infty}\sum_{n=1}^{\infty} J_m(\lambda_{mn}r) \times \left[A_{mn}\cos(m\phi) + B_{mn}\sin(m\phi)\right] \times Z_{mn}(z)T_{mn}(t), \tag{11}$$

where λ_{mn} is the nth root of $J_m(\lambda) = 0$.

To find Z_{mn}, we use the $O(E^{1/2})$ axial flow,

$$\delta v_z^1 = \frac{1}{FN^2}\frac{\partial\Phi}{\partial z} - \Phi, \tag{12}$$

as $\delta v_z^0 = 0$. We require $\delta v_z^1 = 0$ at $z = 0$, so that the flow is symmetric about the mid-plane. The normalization of Z_{mn} is arbitrary, and we choose $Z_{mn}(1) = 1$, giving

$$Z_{mn}(z) = \frac{(FN^2 - \beta_-)\mathrm{e}^{\beta_+ z} - (FN^2 - \beta_+)\mathrm{e}^{\beta_- z}}{(FN^2 - \beta_-)\mathrm{e}^{\beta_+} - (FN^2 - \beta_+)\mathrm{e}^{\beta_-}}, \tag{13}$$

with

$$\beta_\pm = \frac{1}{2}\left[K_s \pm \left(K_s^2 + N^2\lambda_{mn}^2\right)^{1/2}\right]. \tag{14}$$

Another boundary condition applies to the top and bottom faces of the cylinder, which determines T_{mn}. The mass flux into and out of the Ekman boundary layer at $z = \pm 1$ is related to the circulation just outside this layer by (Pedlosky 1967; Walin 1969; Abney & Epstein 1996; van Eysden & Melatos 2008)

$$\delta v_z|_{z=\pm1} = \mp\frac{1}{2}E^{1/2}\left[\nabla\times(\boldsymbol{\delta v} - \boldsymbol{v_B})\right]_z\Big|_{z=\pm1}, \tag{15}$$

where $\boldsymbol{v_B}$ is the dimensionless velocity of the boundary in the frame rotating at Ω. Ekman pumping continues until the local fluid velocity, here $\boldsymbol{\delta v}$, matches the boundary velocity $\boldsymbol{v_B}$. For a rigid container, the final angular velocity equals $\Omega + \delta\Omega$ in the inertial observer's frame, corresponding to $\boldsymbol{v_B} = r\boldsymbol{e}_\phi$ in the rotating frame. To find T_{mn}, we differentiate (15) with respect to time and substitute equation (12) into the left-hand side of (15) (note: $\delta v_z^0 = 0$), and equations (9) and (10) into the right-hand side of (15). After some algebra, we find that the (m, n)th mode relaxes exponentially as $\Phi \propto \exp(-\omega_{mn}t)$, with

$$\omega_{mn} = \frac{\lambda_{mn}^2\left[\left(FN^2 - \beta_-\right)\mathrm{e}^{\beta_+} - \left(FN^2 - \beta_+\right)\mathrm{e}^{\beta_-}\right]}{\left(4FK + \lambda_{mn}^2\right)\left(\mathrm{e}^{\beta_+} - \mathrm{e}^{\beta_-}\right)}. \tag{16}$$

Downloaded from https://academic.oup.com/mnras/article/409/4/1705/986372 by guest on 16 August 2022

Integrating Φ with respect to time, the general solution for the pressure perturbation can be written as

$$\frac{\delta p^0(r,\phi,z,t)}{\rho(z)} = C(r,\phi,z) + F\sum_{m=0}^{\infty}\sum_{n=1}^{\infty} J_m(\lambda_{mn}r) \times (A_{mn}\cos m\phi + B_{mn}\sin m\phi) \times Z_{mn}(z)\mathrm{e}^{-\omega_{mn}t}, \quad (17)$$

where A_{mn} and B_{mn} absorb a factor of ω_{mn}^{-1}, and $C(r, \phi, z)$ is the constant of integration. $C(r, \phi, z)$ is constrained by the boundary condition (15) and must match the boundary velocity at $z = 1$. Using (9) and (10), we obtain

$$v_{Br}(r,\phi,1) = -\frac{1}{2Fr}\frac{\partial C(r,\phi,1)}{\partial\phi}, \quad (18)$$

$$v_{B\phi}(r,\phi,1) = \frac{1}{2F}\frac{\partial C(r,\phi,1)}{\partial r}. \quad (19)$$

2.4 Initial conditions

All that remains is to specify the initial conditions, which determine A_{mn} and B_{mn}. Without specializing to a particular trigger for the spin-up event at $t = 0$ or modelling the vortex unpinning and rearrangement that presumably accompanies it, we consider the general situation where these processes establish some instantaneously non-axisymmetric pressure field throughout the interior. [Five possible physical causes of the non-axisymmetry are discussed in detail in section 1 of van Eysden & Melatos (2008).] We denote the initial state at $t = 0$ by the symbol $\delta P^0(r, \phi, z) = \delta p\,(r, \phi, z, 0)/\rho(z)$. Specifying $\delta P^0(r, \phi, z)$ is equivalent to specifying the initial velocity or density, which are related through (9), (10), (12) and the $O(E^0)$ equation of motion,

$$\delta\rho^0 = -\frac{\partial\delta p^0}{\partial z}. \quad (20)$$

The choice of $\delta P^0(r, \phi, z)$ is arbitrary, but it should satisfy the boundary conditions outlined in Section 2.3. We eliminate $C(r, \phi, z)$ by evaluating (17) at $t = 0$, obtaining

$$\frac{\delta p^0(r,\phi,z,t)}{\rho(z)} = \delta P^0(r,\phi,z) + F\sum_{m=0}^{\infty}\sum_{n=1}^{\infty} J_m(\lambda_{mn}r) \times (A_{mn}\cos m\phi + B_{mn}\sin m\phi) \times Z_{mn}(z)(\mathrm{e}^{-\omega_{mn}t} - 1). \quad (21)$$

The coefficients A_{mn} and B_{mn} are determined at $z = 1$ from $\delta P^0(r, \phi, z)$ and $C(r, \phi, 1)$. In general, we have

$$A_{mn} = \frac{2}{\pi F J_{m+1}^2(\lambda_{mn})}\int_0^{2\pi}\mathrm{d}\phi\int_0^1 \mathrm{d}r\, r\, J_m(\lambda_{mn}r)\cos(m\phi) \times \left[\delta P^0(r,\phi,1) - C(r,\phi,1)\right]. \quad (22)$$

B_{mn} is given by the same formula, with $\cos(m\phi)$ replaced by $\sin(m\phi)$.

2.5 Velocity, density and pressure solutions

Equations (9), (10), (12), (20) and (21) yield complete solutions for the velocity, density and pressure fields. Upon transforming back to dimensional variables and out of the rotating frame into the inertial observer's frame, we can write the results as follows:

$$v_r(r,\phi,z,t) = \delta v_r(r,\phi,z,0) + \frac{1}{2}L^2\delta\Omega\sum_{m=0}^{\infty}\sum_{n=1}^{\infty}\frac{m}{r}J_m(\lambda_{mn}r/L) \times \left[\frac{(FN^2-\beta_-)\mathrm{e}^{\beta_+ z/L} - (FN^2-\beta_+)\mathrm{e}^{\beta_- z/L}}{(FN^2-\beta_-)\mathrm{e}^{\beta_+} - (FN^2-\beta_+)\mathrm{e}^{\beta_-}}\right] \times \{A_{mn}\sin[m(\phi-\Omega t)] - B_{mn}\cos[m(\phi-\Omega t)]\} \times (\mathrm{e}^{-E^{1/2}\omega_{mn}\Omega t} - 1), \quad (23)$$

$$v_\phi(r,\phi,z,t) = \Omega r + \delta v_\phi(r,\phi,z,0) + \frac{1}{2}L\delta\Omega\sum_{m=0}^{\infty}\sum_{n=1}^{\infty}\lambda_{mn}J_m'(\lambda_{mn}r/L) \times \left[\frac{(FN^2-\beta_-)\mathrm{e}^{\beta_+ z/L} - (FN^2-\beta_+)\mathrm{e}^{\beta_- z/L}}{(FN^2-\beta_-)\mathrm{e}^{\beta_+} - (FN^2-\beta_+)\mathrm{e}^{\beta_-}}\right] \times \{A_{mn}\cos[m(\phi-\Omega t)] + B_{mn}\sin[m(\phi-\Omega t)]\} \times (\mathrm{e}^{-E^{1/2}\omega_{mn}\Omega t} - 1), \quad (24)$$

$$v_z(r,\phi,z,t) = \frac{1}{4}L\delta\Omega E^{1/2}\sum_{m=0}^{\infty}\sum_{n=1}^{\infty}\lambda_{mn}^2 J_m(\lambda_{mn}r/L) \times \left(\frac{\mathrm{e}^{\beta_+ z/L} - \mathrm{e}^{\beta_- z/L}}{\mathrm{e}^{\beta_+} - \mathrm{e}^{\beta_-}}\right) \times \{A_{mn}\cos[m(\phi-\Omega t)] + B_{mn}\sin[m(\phi-\Omega t)]\} \times (\mathrm{e}^{-E^{1/2}\omega_{mn}\Omega t} - 1), \quad (25)$$

$$\rho(r,\phi,z,t) = \rho_0\mathrm{e}^{-z/z_s} + \delta\rho(r,\phi,z,0) + \frac{\rho_0 L\Omega\delta\Omega}{g}\sum_{m=0}^{\infty}\sum_{n=1}^{\infty}J_m(\lambda_{mn}r/L) \times \left[\frac{(FN^2-\beta_-)\beta_-\mathrm{e}^{-\beta_- z/L} - (FN^2-\beta_+)\beta_+\mathrm{e}^{-\beta_+ z/L}}{(FN^2-\beta_-)\mathrm{e}^{\beta_+} - (FN^2-\beta_+)\mathrm{e}^{\beta_-}}\right] \times \{A_{mn}\cos[m(\phi-\Omega t)] + B_{mn}\sin[m(\phi-\Omega t)]\} \times (\mathrm{e}^{-E^{1/2}\omega_{mn}\Omega t} - 1), \quad (26)$$

$$p(r,\phi,z,t) = \rho_0 g z_s\mathrm{e}^{-z/z_s} + \delta p(r,\phi,z,0) + \rho_0 L^2\Omega\delta\Omega\sum_{m=0}^{\infty}\sum_{n=1}^{\infty}J_m(\lambda_{mn}r/L) \times \left[\frac{(FN^2-\beta_-)\mathrm{e}^{-\beta_- z/L} - (FN^2-\beta_+)\mathrm{e}^{-\beta_+ z/L}}{(FN^2-\beta_-)\mathrm{e}^{\beta_+} - (FN^2-\beta_+)\mathrm{e}^{\beta_-}}\right] \times \{A_{mn}\cos[m(\phi-\Omega t)] + B_{mn}\sin[m(\phi-\Omega t)]\} \times (\mathrm{e}^{-E^{1/2}\omega_{mn}\Omega t} - 1). \quad (27)$$

The initial velocity, density and pressure are related to the chosen initial state $\delta P^0(r, \phi, z)$ through

$$\delta v_r(r,\phi,z,0) = -\frac{1}{2Fr}\frac{\partial\delta P^0(r,\phi,z)}{\partial\phi}, \quad (28)$$

$$\delta v_\phi(r,\phi,z,0) = \frac{1}{2F}\frac{\partial\delta P^0(r,\phi,z)}{\partial r}, \quad (29)$$

Downloaded from https://academic.oup.com/mnras/article/409/4/1705/986372 by guest on 16 August 2022

$$\delta\rho(r,\phi,z,0) = -\frac{\partial\left[\rho(z)\delta P^0(r,\phi,z)\right]}{\partial z}, \tag{30}$$

$$\delta p(r,\phi,z,0) = \rho(z)\delta P^0(r,\phi,z). \tag{31}$$

In the limit $t \to \infty$, an incompressible fluid spins up completely via Ekman pumping and approaches a steady-state solution, which matches the boundary at $z = 1$. In contrast, for a compressible, stratified fluid, part of the volume is untouched by Ekman pumping. In the latter case, the persistent, unaccelerated initial flow and the associated gradient in v_ϕ dissipate by viscous diffusion and adjust via inertial oscillations over the long time-scale $E^{-1}\Omega^{-1}$.

2.6 $\delta P^0(r, \phi, z)$ for a glitch

In this paper, we assume that a glitch spins up the crust rigidly and axisymmetrically but that it initially excites non-axisymmetric motions in the fluid interior; that is, δv_r^0 and δv_ϕ^0 are superpositions of $\cos(m\phi)$ and $\sin(m\phi)$ modes immediately after the glitch. Possible physical mechanisms are outlined in section 1 of van Eysden & Melatos (2008). The crust spins up rigidly to angular velocity $\Omega + \delta\Omega$, which corresponds to $C(r, \phi, 1) = Fr^2$ in equation (22), satisfying (18) and (19) as required. The arbitrary initial pressure perturbation $\delta P^0(r, \phi, z)$, which specifies the initial flow velocity through (9), (10) and (12), is a sum of non-axisymmetric modes satisfying the boundary conditions (e.g. no penetration of the side walls). In dimensionless form, in the rotating frame, we can write

$$\delta P^0(r,\phi,z) = F\sum_{m=1}^{\infty} C_m r^m (r^2-1)\cos(m\phi). \tag{32}$$

No $\sin(m\phi)$ terms or z dependence are included for simplicity, and the relative weights of the modes are parametrized by the constants C_m. We take $C_m = 1$ for all m in this paper.

The above initial condition is slightly more realistic than the one adopted by van Eysden & Melatos (2008), who posited that the perturbed (spin-up) flow develops from $\delta v_r^0 = \delta v_\phi^0 = 0$ immediately after the glitch to a permanently non-axisymmetric steady-state flow at the boundary [see equations (40) and (41) in van Eysden & Melatos (2008)]. There are two problems with the latter scenario. First, it involves non-axisymmetric, and therefore non-rigid, motion of the top and bottom faces of the cylindrical container, which in reality would exert large stresses on the stellar crust, probably causing it to crack. Second, it artificially emits gravitational radiation in the steady state, even at $t \gg E^{-1}\Omega^{-1}$ (cf. Section 3.2 below).

3 GRAVITATIONAL WAVE SIGNAL

The gravitational radiation generated by the non-axisymmetric spin-up flow in Section 2 is the sum of a mass quadrupole contribution, calculated previously by van Eysden & Melatos (2008), and a current quadrupole contribution. The current quadrupole is typically smaller than the mass quadrupole by a factor of $\sim c/v$. However, using the results of Section 2, the non-axisymmetric velocity perturbation is larger than the density perturbation by a factor of F, implying a wavestrain ratio $h_{\rm mass}/h_{\rm current} \sim Fc/v \sim \Omega\, c/g$. We compute the current quadrupole wavestrain in this paper and refer to van Eysden & Melatos (2008) for the mass quadrupole.

3.1 Current quadrupole

The far-field metric perturbation generated by a superposition of current multipole moments can be written as (Thorne 1980)

$$h_{jk}^{TT} = \frac{G}{c^5 D}\sum_{l=2}^{\infty}\sum_{m=-l}^{l}\frac{\partial^l S^{lm}(t)}{\partial t^l}T_{jk}^{B2,lm} \tag{33}$$

in the transverse, traceless gauge, where t is the retarded time, D is the distance from source to observer and $T_{jk}^{B2,lm}$ is a tensor spherical harmonic which is a function of source orientation. The (l, m)th multipole moment, $S^{lm}(t)$, is given by (Melatos & Peralta 2010)

$$S^{lm} = -\frac{32\pi}{(2l+1)!}\left[\frac{l+2}{2l(l-1)(l+1)}\right]^{1/2} \times \int \mathrm{d}^3\boldsymbol{x}\, r^l \boldsymbol{x}\cdot\mathrm{curl}(\rho\boldsymbol{v})Y^{lm*} \tag{34}$$

for a Newtonian source, where Y^{lm} denotes the usual scalar spherical harmonic. In this paper, we only consider the leading-order, quadrupole ($l = 2$) term. Importantly, S^{2m} depends only on the Fourier mode with frequency $m\Omega$ in the spin-up flow described by equations (23)–(27). In other words, the $l = 2$ metric perturbation is a linear superposition of terms of which each is generated by a unique mode in the spin-up flow.

The plus and cross polarizations of the gravitational wave strain can be expressed compactly in terms of S^{21} and S^{22}. The axisymmetric Ekman flow leads to a quadrupole moment $\partial^2 S^{20}/\partial t^2 = O(E)$, which we neglect in this paper. Denoting the inclination angle between the rotation axis of the star and the observer's line of sight by i, we can write

$$h_+(t) = \frac{G}{2c^5 D}\left(\frac{5}{2\pi}\right)^{1/2} \times \{\mathrm{Im}[\ddot{S}^{21}(t)]\sin i + \mathrm{Im}[\ddot{S}^{22}(t)]\cos i\}, \tag{35}$$

$$h_\times(t) = \frac{G}{4c^5 D}\left(\frac{5}{2\pi}\right)^{1/2} \times \{\mathrm{Re}[\ddot{S}^{21}(t)]\sin 2i + \mathrm{Re}[\ddot{S}^{22}(t)](1+\cos^2 i)\}, \tag{36}$$

where the overdots symbolize differentiation with respect to time.

3.2 Gravitational wave strain

We compute the far-field metric perturbation at a hypothetical detector by combining the flow solutions in Section 2.5 with the boundary and initial conditions in Section 2.6. Appendix A shows how to rewrite the integral in (34) to involve only the pressure perturbation δp^0, simplifying the evaluation of S^{lm}. The final result for the current quadrupole moment, for $0 < m \leq 2$, takes the form

$$S^{2m}(t) = \frac{(-1)^{m+1}8\pi(10\pi)^{1/2}}{15m}\rho_0 L^6\delta\Omega \times \sum_{n=1}^{\infty}\left[(U_{mn}-V_{mn})\mathrm{e}^{-im\Omega t} + V_{mn}\mathrm{e}^{-(E^{1/2}\omega_{mn}+im)\Omega t}\right], \tag{37}$$

with

$$U_{mn} = \delta_{n,1}\int_0^1 \mathrm{d}r\int_0^1 \mathrm{d}z\, r^{m+1}z^{2-m}\hat{U}r^m(r^2-1)\mathrm{e}^{-K_s z}, \tag{38}$$

Downloaded from https://academic.oup.com/mnras/article/409/4/1705/986372 by guest on 16 August 2022

$$V_{mn} = \int_0^1 \mathrm{d}r \int_0^1 \mathrm{d}z\, r^{m+1} z^{2-m} \hat{U} A_{mn} J_m(\lambda_{mn} r) \times \left[\frac{(FN^2 - \beta_-)\mathrm{e}^{-\beta_- z} - (FN^2 - \beta_+)\mathrm{e}^{-\beta_+ z}}{(FN^2 - \beta_-)\mathrm{e}^{\beta_+} - (FN^2 - \beta_+)\mathrm{e}^{\beta_-}} \right], \tag{39}$$

where

$$\hat{U} = z\frac{\partial^2}{\partial r^2} + \frac{z}{r}\frac{\partial}{\partial r} - \frac{zm^2}{r^2} - r\frac{\partial^2}{\partial r \partial z} + 2F\left(r^2 \frac{\partial^2}{\partial z^2} - rz\frac{\partial^2}{\partial r \partial z} - 2z\frac{\partial}{\partial z} \right) \tag{40}$$

is a differential operator acting on everything to its right in equations (38) and (39). U_{mn} and V_{mn} are straightforward to calculate analytically, but the full expressions are too lengthy to quote here.

Substituting (37) into (35) and (36), we obtain the following expressions for the plus- and cross-polarizations as functions of time:

$$h_+(t) = h_0 \sum_{n=1}^{\infty} \Bigg[\sin i \Big\{ (U_{1n} - V_{1n}) \sin \Omega t + V_{1n} \mathrm{e}^{-E^{1/2}\omega_{1n}\Omega t} \times \left[2E^{1/2}\omega_{1n} \cos \Omega t - \left(E\omega_{1n}^2 - 1 \right) \sin \Omega t \right] \Big\} - \frac{1}{2} \cos i \Big\{ 4(U_{2n} - V_{2n}) \sin 2\Omega t + V_{2n} \mathrm{e}^{-E^{1/2}\omega_{2n}\Omega t} \times \left[4E^{1/2}\omega_{2n} \cos 2\Omega t - \left(E\omega_{2n}^2 - 4 \right) \sin 2\Omega t \right] \Big\} \Bigg], \tag{41}$$

$$h_\times(t) = \frac{h_0}{2} \sum_{n=1}^{\infty} \Bigg[\sin 2i \Big\{ (V_{1n} - U_{1n}) \cos \Omega t + V_{1n} \mathrm{e}^{-E^{1/2}\omega_{1n}\Omega t} \times \left[\left(E\omega_{1n}^2 - 1 \right) \cos \Omega t + 2E^{1/2}\omega_{1n} \sin \Omega t \right] \Big\} - \frac{1}{2}(1 + \cos^2 i) \Big\{ 4(V_{2n} - U_{2n}) \cos 2\Omega t + V_{2n} \mathrm{e}^{-E^{1/2}\omega_{2n}\Omega t} \times \left[\left(E\omega_{2n}^2 - 4 \right) \cos 2\Omega t + 4E^{1/2}\omega_{2n} \sin 2\Omega t \right] \Big\} \Bigg], \tag{42}$$

with

$$h_0 = \frac{4\pi G \rho_0 L^6 \delta\Omega\, \Omega^2}{3c^5 D}. \tag{43}$$

Equations (41) and (42) contain terms of order $(E\omega_{mn}^2)^0$, $(E\omega_{mn}^2)^{1/2}$ and $(E\omega_{mn}^2)^1$. The derivation of the spin-up flow in Section 2 assumes $E^{1/2} \ll 1$. Over the range of values for K, N and E that we consider in Sections 4 and 5, it is also true that $E^{1/2}\omega_{m1} \ll 1$. The quantity $E^{1/2}\omega_{mn}$ does become large for large n ($\omega_{mn} \to n\pi/2$ as $n \to \infty$), but the exponential suppresses the large-n terms and the infinite sum converges. For our purposes, truncating (41) and (42) at leading order $O(E^0)$ gives a good approximation.

In the scenario described in Section 2.6, the non-axisymmetric initial perturbation is erased by Ekman pumping on the time-scale t_E, and the fluid spins up to rotate axisymmetrically with the boundary at $z = 1$. The effects of stratification and compressibility reduce the effectiveness of Ekman pumping, reducing the spin-up volume. As a result, some regions of the interior are incompletely spun up and preserve some of their initial non-axisymmetric flow for $t \gg t_E$, unlike in the incompressible problem. The non-axisymmetry persists, emitting gravitational radiation continuously, until viscous diffusion wipes it out on the time-scale $E^{-1}\Omega^{-1}$ (Greenspan & Howard 1963; Benton & Clark 1974). As the time-scale $E^{-1}\Omega^{-1} \gtrsim 10^3$ yr is comparable to, or greater than, the age of many glitching pulsars, one encounters the interesting possibility that neutron stars harbour a 'fossil' non-axisymmetric flow in their interior, preserved by stratification, which continually emits gravitational radiation, and whose structure reflects the history of differential rotation and superfluid vortex rearrangement in the star. This possibility merits careful investigation in the future. It is not the same as the artificial, non-axisymmetric, non-rigid rotation of the crust postulated (for mathematical convenience) by van Eysden & Melatos (2008) (cf. also Section 2.6).

4 DETECTABILITY

We now estimate the detectability of the gravitational wave signal derived in Section 3 by calculating the signal-to-noise ratio expected to be achieved by current- and next-generation long-baseline interferometers. The signal differs from a traditional continuous-wave source (e.g. an elliptical neutron star), because it decays over days to weeks (approximately 10^5–10^8 wave cycles). It is therefore counterproductive to integrate coherently past a certain time (if one ignores the fossil quadrupole discussed in Section 3.2). We find that the signal-to-noise ratio depends sensitively on the buoyancy, compressibility and viscosity of the neutron star interior. For certain, plausible ranges of these variables, the signal is detectable in principle by Advanced LIGO.

4.1 Signal-to-noise ratio

The response of a laser interferometer to plus- and cross-polarizations $h_+(t)$ and $h_\times(t)$ can be written as

$$h(t) = F_+(t)h_+(t) + F_\times(t)h_\times(t). \tag{44}$$

The beam-pattern functions F_+ and $F_\times$ depend on the rotation of the Earth and the sky position of the source (Jaranowski, Królak & Schutz 1998). For the signal in Section 3, it is convenient to split $h(t)$ into components that oscillate at the spin frequency of the star and its first harmonic, denoted by $h_1(t)$ and $h_2(t)$, respectively. Writing $h_{1,2}(t) = F_+(t)\, h_{1,2+}(t) + F_\times(t)\, h_{1,2\times}(t)$ and keeping terms of order $O(E^0)$ in (41) and (42), we find

$$h_{1+}(t) = h_0 \sin i \sin \Omega t \times \sum_{n=1}^{\infty} \left(U_{1n} - V_{1n} + V_{1n} \mathrm{e}^{-E^{1/2}\omega_{1n}\Omega t} \right), \tag{45}$$

$$h_{2+}(t) = -2h_0 \cos i \sin 2\Omega t \times \sum_{n=1}^{\infty} \left(U_{2n} - V_{2n} + V_{2n} \mathrm{e}^{-E^{1/2}\omega_{2n}\Omega t} \right), \tag{46}$$

$$h_{1\times}(t) = -\frac{h_0}{2} \sin 2i \cos \Omega t \times \sum_{n=1}^{\infty} \left(U_{1n} - V_{1n} + V_{1n} \mathrm{e}^{-E^{1/2}\omega_{1n}\Omega t} \right), \tag{47}$$

$$h_{2\times}(t) = h_0(1 + \cos^2 i) \cos 2\Omega t \times \sum_{n=1}^{\infty} \left(U_{2n} - V_{2n} + V_{2n} \mathrm{e}^{-E^{1/2}\omega_{2n}\Omega t} \right). \tag{48}$$

Downloaded from https://academic.oup.com/mnras/article/409/4/1705/986372 by guest on 16 August 2022

The signal-to-noise ratio d for a quasi-dichromatic source (i.e. a source consisting of two narrow-band peaks at frequencies f_* and $2f_*$) is given by equations (80)–(82) in Jaranowski et al. (1998). The result is

$$d^2 = \frac{2}{S_h(f_*)} \int_{-T_0/2}^{T_0/2} \mathrm{d}t\, [h_1(t)]^2 + \frac{2}{S_h(2f_*)} \int_{-T_0/2}^{T_0/2} \mathrm{d}t\, [h_2(t)]^2 \,. \quad (49)$$

In (49), $S_h(f)$ is the spectral noise density of the interferometer at frequency f, T_0 denotes the total length of the coherent integration, and $f_* = \Omega/2\pi$ is the stellar spin frequency.

The integration time for a coherent search is normally limited by computational expense rather than the length of the data stream. Even when the radio ephemeris is known through radio observations, the radio and gravitational wave phases may not be equal, increasing the number of templates required for a search [e.g. the $\mathcal{F}$-statistic search for the Crab (Abbott et al. 2008)]. We assume a computational limit of two weeks for the remainder of this paper. For the glitch recovery signal, the integration time is the minimum of the computational limit and the glitch recovery time-scale; integrating beyond the point where the signal decays away merely adds noise. The exact value of T_0 which maximizes d depends on the search algorithm, but it is always of order the e^{-1} time constant for $h(t)$, i.e. $h(T_0)/h(0) = \mathrm{e}^{-1}$. For the general estimates below, we take $T_0 = (E^{1/2}\omega_{21}\Omega)^{-1}$, the e^{-1} decay time-scale of the leading ($n = 1$) term in equations (45)–(48). The $m = 2$ mode decays more quickly than the $m = 1$ mode, but the difference is moderate ($1 \leq \omega_{21}/\omega_{11} \leq 2$) over the parameter space that we consider.

Fig. 1 illustrates how T_0 depends on stellar parameters. The four panels in Fig. 1 display contours of T_0 (in days) on the K-N plane for four different values of E. The value of E in a neutron star is uncertain but Fig. 1 demonstrates that it plays a significant role in determining T_0. One requires $E \sim 10^{-17}$ for the best match between $(E^{1/2}\omega_{21}\Omega)^{-1}$ and observed post-glitch recovery time-scales. This value is artificially lower than that expected from neutron–neutron scattering, $E \sim 10^{-7}(\Omega/\mathrm{rads}^{-1})^{-1}$ (Cutler & Lindblom 1987; Andersson et al. 2005; van Eysden & Melatos 2010) because it is the effective value that arises when modelling the two-component Hall–Vinen–Bekarevich–Khalatnikov superfluid (Peralta et al. 2005; Andersson & Comer 2006) as a single Newtonian fluid (Easson 1979; Abney & Epstein 1996; van Eysden & Melatos 2008).

To calculate d, we evaluate (49) with $T_0 = (E^{1/2}\omega_{21}\Omega)^{-1}$ and make several simplifying assumptions. First, we approximate $h(t)$ by the leading ($n = 1$) terms in the infinite sums in (45)–(48). For typical values of N and K, this introduces an error of $\lesssim$10 per cent. Second, following Jaranowski et al. (1998), we average the functions $\sin(m\Omega t)$ and $\cos(m\Omega t)$, which oscillate much more rapidly than F_+, $F_\times$, and $\exp(-t/T_0)$, over the observation period. The result is

$$\begin{aligned} d^2 = {} & \frac{(1-\mathrm{e}^{-2})h_0^2 A_1(K,N)}{S_h(f_*)} \\ & \times \int_0^{T_0} \mathrm{d}t \left[\sin^2 i\ F_+^2 + \frac{1}{4}\sin^2 2i\ F_\times^2\right] \\ & + \frac{(1-\mathrm{e}^{-2})h_0^2 A_2(K,N)}{S_h(2f_*)} \\ & \times \int_0^{T_0} \mathrm{d}t \left[4\cos^2 i\ F_+^2 + (1+\cos^2 i)^2\ F_\times^2\right], \end{aligned} \quad (50)$$

with

$$\begin{aligned} A_i(K,N) = {} & \frac{1}{1-\mathrm{e}^{-2}}(U_{i1} - V_{i1})^2 \\ & + \frac{2\mathrm{e}}{1+\mathrm{e}}(U_{i1} - V_{i1})V_{i1} + \frac{1}{2}V_{i1}^2. \end{aligned} \quad (51)$$

As discussed in Section 3.2, the signal is the sum of a persistent periodic signal associated with the fossil non-axisymmetry (which decays on the long time-scale $E^{-1}\Omega^{-1} \gg T_0$) and the decaying signal generated by the Ekman flow. To be conservative, we only consider the latter signal, setting $U_{mn} = V_{mn}$. Hence, (51) reduces to $A_i(K,N) = V_{i1}^2/2$.

The signal-to-noise ratio depends on the right ascension α, declination δ and polarization angle ψ of the source as well as the location and orientation of the interferometer and the diurnal phase of the Earth. These quantities are usually known for any specific

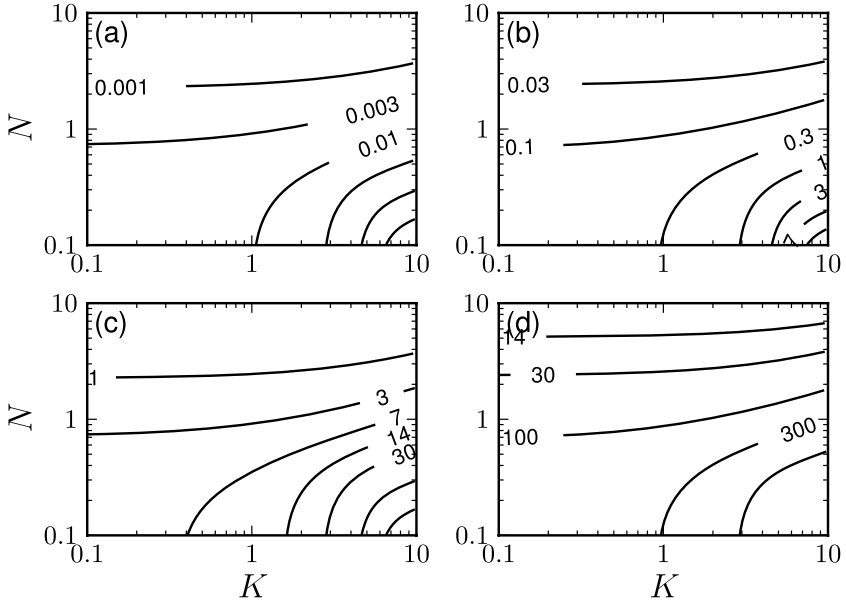

Figure 1. Contours of integration time T_0 (in days) as a function of the normalized compressibility K and Brunt–Väisälä frequency N. The integration time is chosen such that $h(t = T_0) = \mathrm{e}^{-1}\, h(t = 0)$. The Ekman number increases from the top left to the bottom right panels: (a) $E = 10^{-11}$, (b) $E = 10^{-14}$, (c) $E = 10^{-17}$, (d) $E = 10^{-20}$.

© 2010 The Authors. Journal compilation © 2010 RAS, MNRAS **409,** 1705–1718

Downloaded from https://academic.oup.com/mnras/article/409/4/1705/986372 by guest on 16 August 2022

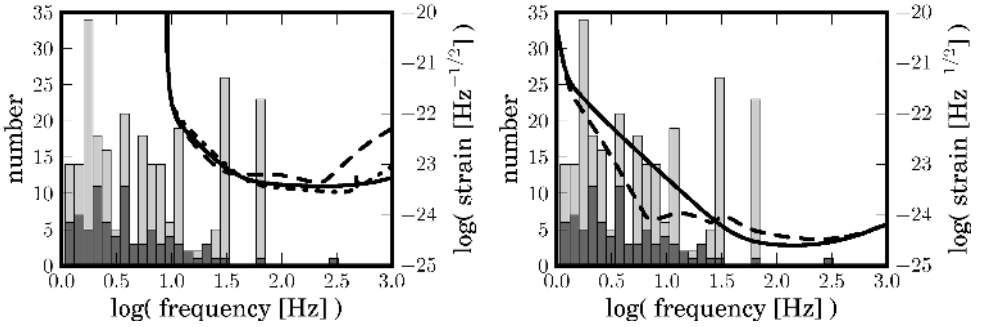

Figure 2. Histogram of known glitching pulsars (dark shading) and observed glitches (light shading) as a function of frequency. Curves of anticipated spectral noise density for second- and third-generation interferometers are overlaid. [Note: glitches emit gravitational radiation at both f_* and $2f_*$ (see Section 3).] Left panel displays Advanced LIGO configurations: zero detuning, high power (solid), black hole optimized (dashed), neutron star optimized (dash-dotted). Right panel displays ET configurations: conventional (solid), xylophone (dashed).

source. However, to estimate detectability in general, we average d over α, δ, ψ and i (Jaranowski et al. 1998):

$$\langle \ldots \rangle_{\alpha,\delta,\psi,i} = \frac{1}{2\pi}\int_0^{2\pi} \mathrm{d}\alpha \times \frac{1}{2}\int_{-1}^{1} \mathrm{d}(\sin\delta) \times \frac{1}{2\pi}\int_0^{2\pi} \mathrm{d}\psi \times \frac{1}{2}\int_{-1}^{1} \mathrm{d}(\cos i)\,(\ldots). \quad (52)$$

The beam pattern functions average to

$$\left\langle \int_0^{T_0} \mathrm{d}t\, F_+^2 \right\rangle_{\alpha,\delta,\psi} = \left\langle \int_0^{T_0} \mathrm{d}t\, F_\times^2 \right\rangle_{\alpha,\delta,\psi} = \frac{T_0}{5}\sin^2\zeta, \quad (53)$$

where ζ is the angle between the arms of the detector. We give more details of this result in Appendix B. Substituting (53) into (51) and averaging over i, we obtain the following expression for the average signal-to-noise ratio:

$$\langle d \rangle_{\alpha,\delta,\psi,i} = \frac{2}{5}(1-\mathrm{e}^{-2})^{1/2} h_0\, T_0^{1/2} \sin\zeta \times \left[\frac{A_1(K,N)}{S_h(f_*)} + \frac{4A_2(K,N)}{S_h(2f_*)}\right]^{1/2}. \quad (54)$$

4.2 Second- and third-generation interferometers

We now evaluate the signal-to-noise ratio (54) achieved by the second-generation interferometer LIGO, in both its Initial and Advanced configurations, and the third-generation, subterranean Einstein Telescope (ET).

There are various detector configurations proposed for Advanced LIGO[1]. The best overall sensitivity across the entire frequency spectrum is achieved with zero detuning of the signal recycling mirror and high laser power. Below 40 Hz, the configuration optimized for 30 $\mathrm{M}_\odot$ black hole binary inspirals provides the best sensitivity. Above 40 Hz, the configuration optimized for 1.4 $\mathrm{M}_\odot$ neutron star binary inspirals provides the best sensitivity. However, the differences between the three configurations are small.

Two configurations have been proposed for ET: a conventional interferometer (Hild, Chelkowski & Freise 2008), and a dual-band xylophone configuration consisting of two colocated interferometers, one optimized for low frequencies and the other for high frequencies (Hild et al. 2010). Below 30 Hz, the xylophone configuration is more sensitive than the conventional configuration, by a factor of up to ∼10 in the 5–10 Hz band.

[1] LIGO Document Control Center: document number LIGO-T0900288-v3

Fig. 2 compares the spectral noise density of the different detector configurations. It also bins the number of known glitching pulsars and observed glitches as a function of frequency to illustrate which configurations are best suited for glitch searches. It is important to recall that the results of Section 3 predict gravitational radiation at both the pulsar frequency f_* and $2f_*$, with the pulsar orientation determining which frequency has the stronger signal. The xylophone configuration of ET is the best choice for a glitch search. More glitches have been observed in objects with $f < 30$ Hz (83 per cent), where the xylophone is more sensitive, than $f > 30$ Hz (17 per cent) (Peralta 2006; Melatos et al. 2008). Additionally, the increase in sensitivity of the ET xylophone configuration over the conventional configuration is far greater below 30 Hz than the decrease above 30 Hz. In contrast, Advanced LIGO is not sensitive below 10 Hz and there is only a small difference in sensitivity between the different configurations over the frequency range where most glitches lie. As mentioned above, the black-hole-optimized Advanced LIGO configuration is the most sensitive below 40 Hz but its advantage is slight and possibly outweighed by its slightly poorer performance at higher frequencies, where the strongest signals (from the fastest-spinning objects) arguably lie.

Fig. 3 displays contours of the average signal-to-noise ratio for Initial LIGO, Advanced LIGO (zero detuning and high laser power, neutron star optimized and black hole optimized), and ET (conventional and xylophone) as a function of compressibility K and Brunt–Väisälä frequency N. The figure is produced for an object with $f_* = 100$ Hz, $E = 10^{-17}$, at a distance $D = 1$ kpc from Earth, with radius $R = 10$ km, mass $M = 1.4\ \mathrm{M}_\odot$, $\rho_0 = 3M/4\pi R^3$ and $g = GM/R^2$ (Ekman pumping occurs in a thin surface layer, where g is uniform). The step increase in angular velocity is taken to be $\delta\Omega/\Omega = 2 \times 10^{-4}$, corresponding to the largest glitch observed to date (Melatos et al. 2008). The spectral noise densities $[S_h(f_*), S_h(2f_*)]$ used for the six detector configurations are: Initial LIGO ($1.74 \times 10^{-45}\,\mathrm{Hz}^{-1}$, $8.54 \times 10^{-46}\,\mathrm{Hz}^{-1}$); zero-detuning, high-power Advanced LIGO ($1.59 \times 10^{-47}\,\mathrm{Hz}^{-1}$, $1.39 \times 10^{-47}\,\mathrm{Hz}^{-1}$); neutron-star-optimized Advanced LIGO ($1.18 \times 10^{-47}\,\mathrm{Hz}^{-1}$, $9.03 \times 10^{-48}\,\mathrm{Hz}^{-1}$); black-hole-optimized Advanced LIGO ($3.77 \times 10^{-47}\,\mathrm{Hz}^{-1}$, $1.84 \times 10^{-47}\,\mathrm{Hz}^{-1}$); conventional ET ($6.68 \times 10^{-50}\,\mathrm{Hz}^{-1}$, $6.68 \times 10^{-50}\,\mathrm{Hz}^{-1}$); and xylophone ET ($1.56 \times 10^{-49}\,\mathrm{Hz}^{-1}$, $1.12 \times 10^{-49}\,\mathrm{Hz}^{-1}$).

It is clear from Fig. 3 that detectability drops off sharply for $K > 10$. Buoyancy prevents Ekman pumping from spinning up the whole of the stellar interior (van Eysden & Melatos 2008). For large stratification ($K_s \gg FN^2$), $K_s \approx K$, only a small volume of the interior is spun up and the current quadrupole is greatly

Downloaded from https://academic.oup.com/mnras/article/409/4/1705/986372 by guest on 16 August 2022

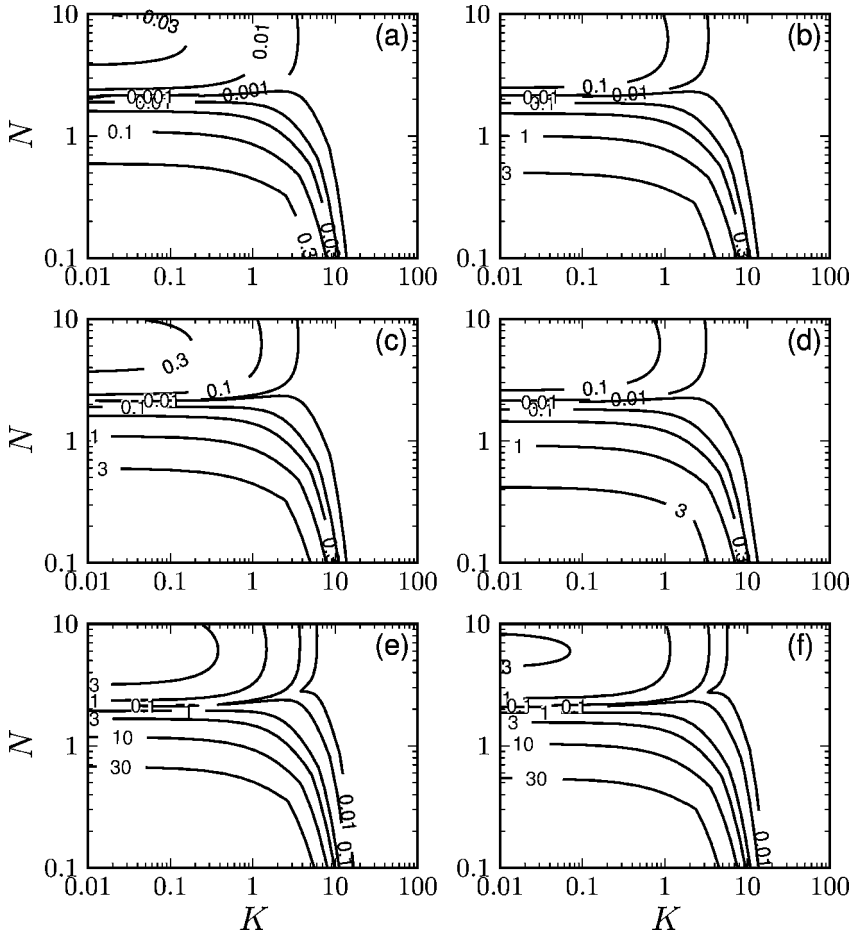

Figure 3. Contours of angle-averaged signal-to-noise ratio $\langle d\rangle$ versus normalized compressibility K and Brunt–Väisälä frequency N, for four existing and planned interferometers: (a) Initial LIGO; (b) Zero-detuning, high-power Advanced LIGO; (c) Neutron star optimized Advanced LIGO; (d) Black hole optimized Advanced LIGO; (e) Conventional ET; (f) Xylophone ET. Source parameters: $f_* = 100$ Hz, $\delta\Omega/\Omega = 2 \times 10^{-4}$, $E = 10^{-17}$, $D = 1$ kpc. The detector spectral noise densities used are $(S_h(f_*), S_h(2f_*))$: Initial LIGO ($1.75 \times 10^{-45}\,\mathrm{Hz}^{-1}$, $8.53 \times 10^{-46}\,\mathrm{Hz}^{-1}$); zero-detuning, high-power Advanced LIGO ($1.59 \times 10^{-47}\,\mathrm{Hz}^{-1}$, $1.39 \times 10^{-47}\,\mathrm{Hz}^{-1}$); neutron-star-optimized Advanced LIGO ($1.18 \times 10^{-47}\,\mathrm{Hz}^{-1}$, $9.03 \times 10^{-48}\,\mathrm{Hz}^{-1}$); black-hole-optimized Advanced LIGO ($3.77 \times 10^{-47}\,\mathrm{Hz}^{-1}$, $1.84 \times 10^{-47}\,\mathrm{Hz}^{-1}$); conventional ET ($6.68 \times 10^{-50}\,\mathrm{Hz}^{-1}$, $6.68 \times 10^{-50}\,\mathrm{Hz}^{-1}$); and xylophone ET ($1.56 \times 10^{-49}\,\mathrm{Hz}^{-1}$, $1.12 \times 10^{-49}\,\mathrm{Hz}^{-1}$).

reduced, with $A_{1,2} \propto \mathrm{e}^{-2K}$. There is little difference between the three Advanced LIGO configurations in panels (b)–(d), or the two ET configurations displayed in panels (e) and (f) in Fig. 3. All have similar sensitivity at 100 Hz. For ET, we find $\langle d\rangle \gtrsim 3$ for $K \lesssim 10$ and $N \lesssim 1$ and there is a reasonable possibility of detection. We require smaller values, e.g. $N \lesssim 0.5$ and $K \lesssim 3$, to achieve $\langle d\rangle \gtrsim 3$ with Advanced LIGO.

To generalize the results in Fig. 3 to an arbitrary object, we note that $\langle d\rangle$ scales with Ekman number as $\langle d\rangle \propto E^{1/4}$ (square root of the number of cycles in the coherent integration). For relaxation time-scales of 3–300 d (Peralta 2006), and assuming $K = N = 1$, E ranges from 10^{-21} to 10^{-17}, which corresponds to an order of magnitude of variation in $\langle d\rangle$. The signal-to-noise ratio also scales with the spin parameters through the characteristic wavestrain, viz.

$$h_0 = 6 \times 10^{-26} \left(\frac{\delta\Omega/\Omega}{10^{-4}}\right) \left(\frac{f_*}{10^2\,\mathrm{Hz}}\right)^3 \left(\frac{D}{1\,\mathrm{kpc}}\right)^{-1}. \quad (55)$$

The relative change in angular velocity $\delta\Omega/\Omega$ is not necessarily equal to the observed glitch size $\delta\nu/\nu$. In a vortex unpinning model, the two quantities are related through $\delta\nu/\nu \sim (I_s/I_c)(\Delta r/R)(\delta\Omega/\Omega)$, where $I_s/I_c \sim 10^2$ is the ratio of superfluid to crust moment of inertia, and $\Delta r/R \sim 10^{-6}$ is the normalized radial distance the unpinned vortices move (Alpar, Nandkumar & Pines 1986; Melatos & Peralta 2010). Therefore, equating the observed glitch size to $\delta\Omega/\Omega$ yields a conservative estimate, given that $\delta\Omega/\Omega$ may in fact be up to $\sim 10^4$ times larger.

A coherent search synchronized to a radio ephemeris assumes that the radio and gravitational wave signals have the same phase. This is not necessarily true. For example, in the landmark coherent $\mathcal{F}$-statistic search for the Crab pulsar in LIGO S5 data, Abbott et al. (2008) allowed for a fractional phase mismatch of up to 10^{-4}. In our multiple scales analysis, we assume by construction that the non-axisymmetric modes are stationary in the frame rotating with the pre-glitch angular velocity and remain so throughout the Ekman pumping process. In reality, the crust spins up to $\Omega + \delta\Omega$ and drags the axisymmetric part of the flow asymptotically to this increased angular velocity. Whether the angular velocity of the $m \neq 0$ modes also increases during this process is unclear. It depends on exactly how the superfluid vortices repin following a glitch and rearrange themselves in a sheared Ekman flow, which is unknown at present.

The number of templates required for a search can be estimated by modelling the frequency as $f(t) = f_0 + \dot{f}_0 t$. For a coherent

Downloaded from https://academic.oup.com/mnras/article/409/4/1705/986372 by guest on 16 August 2022

search, the difference in phase between the model and gravitational wave signals over the integration time must satisfy $\Delta\varphi < \pi$. For a two-week integration, this corresponds to a maximum template spacing of $\delta f_0 = 3 \times 10^{-6}$ Hz and $\delta \dot{f}_0 = 4 \times 10^{-12}\,\mathrm{s}^{-2}$.

During the glitch recovery, the frequency derivative is much larger than usual for an isolated pulsar spinning down electromagnetically. We approximate $\dot{f}_0 \approx \Delta\nu/T_0$. Conservatively, this yields $\dot{f}_0 \sim 10^{-7}\,\mathrm{s}^{-2}$ for a 100-Hz pulsar undergoing the largest glitch observed to date ($\Delta\nu/\nu \sim 10^{-4}$) with an unusually short relaxation period of 1 d. This translates into a range of $\Delta \dot{f}_0 = 10^{-7}\,\mathrm{s}^{-2}$ to search over and hence 3×10^4 templates in $\dot{f}_0$. To allow for some mismatch between the radio and gravitational wave phases, we follow Abbott et al. (2008) who searched over a window of $\pm 6 \times 10^{-3}$ Hz centred on the radio frequency, i.e. $\Delta f_0 = 1.2 \times 10^{-2}$ Hz. Overall, therefore, a total of $\sim 10^8$ templates are required for a glitch search.

The parameters N, K and E change the shape of the signal in two ways: the relaxation time is controlled predominantly by E, while the relative difference between the signals at f_* and $2f_*$ (in amplitude and relaxation time) is controlled by N and K. Our signal-to-noise ratio estimates in Fig. 3 are based on the incoherent sum of the detector response at f_* and $2f_*$, so the relative phasing between f_* and $2f_*$ does not affect the detectability and the number of templates required. This would change in a more sophisticated search that combined the f_* and $2f_*$ responses coherently.

To this point, we assume that radio observations provide the frequency, recovery time-scale and trigger epoch for a glitch search. We now consider the scenario where this information is not known, as in a blind search. In the region of parameter space that we consider, $0.1 \leq N \leq 10$, $0.1 \leq K \leq 10$ and $10^{-20} \leq E \leq 10^{-8}$, the minimum bandwidth of the Fourier-transformed wavestrain is $\approx 6 \times 10^{-12} f_*$. Hence, searching over the frequency range 1–600 Hz requires $\sim 10^{12}$ templates in f_0 multiplied by $\sim 10^4$ templates in $\dot{f}_0$ as discussed above.

In addition, the sky position, time of occurrence and recovery time are unknown for a blind search. In a LIGO search for unknown periodic sources (Abbott et al. 2007b), the sky is divided into 31 500 patches. The lack of an electromagnetic trigger means that the data must be searched in many blocks, starting, for example, 1 d apart (coherent integration over a shorter recovery time is unlikely to be detectable) and integrating over increasing lengths of time, up to the computational limit, to account for the fact that T_0 is unknown. A proper estimate of the associated computational expense lies outside the scope of this paper.

5 CONSTITUTIVE PROPERTIES OF BULK NUCLEAR MATTER

Fig. 3 clearly demonstrates that the strength of the gravitational wave signal depends sensitively on the constitutive properties of bulk nuclear matter (e.g. the equation of state) and its dissipative or transport coefficients (e.g. viscosity). We show that these properties can be inferred in principle from the detailed shape of the gravitational wave signal. The results of this approach can be linked to terrestrial experiments, e.g. with heavy ion colliders, although there is an important distinction between $\sim$ GeV collisions of $\sim 10^2$ nucleons in a terrestrial particle accelerator and $\sim 10^{57}$ static nucleons at $\sim$ MeV energies in a neutron star.

In a real search, one seeks to extract parameters like K and N by fitting a template to the interferometer data in the time domain (Clark et al. 2007; Hayama et al. 2008). However, to illustrate the scientific potential of the fitting exercise, we Fourier transform $h_+(t)$ and $h_\times(t)$ and focus on the gross features of the spectrum. We neglect the permanent fossil quadrupole (see Section 3.2) and assume that there is no interference between peaks. The four peak amplitudes and four peak widths (at f_* and $2f_*$) of $h_+(f)$ and $h_\times(f)$ provide enough information to solve for K, N, E, i and h_0 by matching to the theoretical predictions in (45)–(48). We take ratios to eliminate h_0 (which depends on the unknowns ρ_0, R, $\delta\Omega$ and D) and focus on the remaining parameters.

Fig. 4 displays six slices through the four-dimensional parameter space. Contours are shown for the amplitude ratio $|h_+(f_*)|/|h_+(2f_*)|$ and the width ratio $\Gamma_+(f_*)/\Gamma_+(2f_*)$, where $\Gamma_{+,\times}(f_*)$ is the full width at half-maximum of the peak in $|h_{+,\times}(f)|$ centred at f_*. The figure is drawn for the parameter ranges $0.1 \leq K \leq 10$, $0.1 \leq N \leq 10$, $10^{-20} \leq E \leq 10^{-8}$ and $0 \leq i \leq \pi$. We evaluate the first 20 terms in the infinite sums in (45)–(48). In those panels where K, N, E and i are held fixed, we use the fiducial values $K = 1$, $N = 1$, $E = 10^{-17}$ and $i = \pi/4$, respectively.

The inclination angle determines the relative strength of the $m = 1$ and $m = 2$ modes of h_+ and $h_\times$ through the tensor spherical harmonic $T^{B2,lm}_{jk}$ in (33). The contours of $|h_+(f_*)|/|h_+(2f_*)|$ are nearly vertical in panels (d), (e) and (f) of Fig. 4. In fact, if we consider additional amplitude ratios, we can infer i independently from the other parameters. Dividing the Fourier transforms of (45) by (47), and (46) by (48), we obtain $|h_+(f_*)|/|h_\times(f_*)| = \sec i$ and $|h_+(2f_*)|/|h_\times(2f_*)| = 2\cos i/(1 + \cos^2 i)$, respectively. These expressions overdetermine i, yielding its value and an independent cross-check. The inclination angle can also be inferred from the radio or gamma-ray pulse profile and polarization swing by assuming a particular emission model (Lyne & Manchester 1988; Hibschman & Arons 2001; Bai & Spitkovsky 2010; Chung & Melatos, in preparation). The width ratios are independent of i; the time-scale over which the signal decays does not depend on the location of the observer. This is illustrated in panels (d)–(f) of Fig. 4, where the contours of $\Gamma_+(f_*)/\Gamma_+(2f_*)$ are horizontal.

The compressibility K and Brunt–Väisälä frequency N are inextricably linked in the sense that they feed into both the amplitude and width ratios in a complicated manner. However, once we determine i according to the formula above, we can immediately extract K and N from panel (a) of Fig. 4 as the value of E does not influence any of the amplitude or width ratios (see below). By plotting contours of the measured ratios of $|h_+(f_*)|/|h_+(2f_*)|$ and $\Gamma_+(f_*)/\Gamma_+(2f_*)$ on the K-N plane, we can read off the values of N and K from the intersection point of the contours. One might be tempted to use other amplitude and width ratios as a cross-check on K and N, or to break the degeneracy in the case of multiple intersection points. However, most of the ratios are related trivially through the inclination angle and supply no additional information, e.g. $\Gamma_\times(f_*) = \Gamma_+(f_*)$, $\Gamma_\times(2f_*) = \Gamma_+(2f_*)$, $|h_\times(f_+)| = \cos i\,|h_+(f_+)|$ and $|h_\times(2f_+)| = (\cos i + \sec i)|h_+(2f_+)|/2$.

The Ekman number E is important in determining the recovery time-scale and hence the Fourier width. It also appears in h_0 through T_0. However, it influences all peaks in the same way and drops out of all amplitude and width ratios. In panels (b), (c) and (f) of Fig. 4, the amplitude and width ratio contours are vertical. As mentioned in Section 4, an approximate value of E can be inferred from the e-folding time of $h(t)$, as K and N only weakly influence this quantity. However, if K and N are known, e.g. by following the procedure described in the above paragraph, we can determine E from the absolute peak widths. Finally, h_0 can be determined from the absolute peak amplitudes once the values of all the other parameters are known.

Future gravitational wave measurements of the compressibility, viscosity and Brunt–Väisälä frequency of bulk nuclear matter can

Downloaded from https://academic.oup.com/mnras/article/409/4/1705/986372 by guest on 16 August 2022

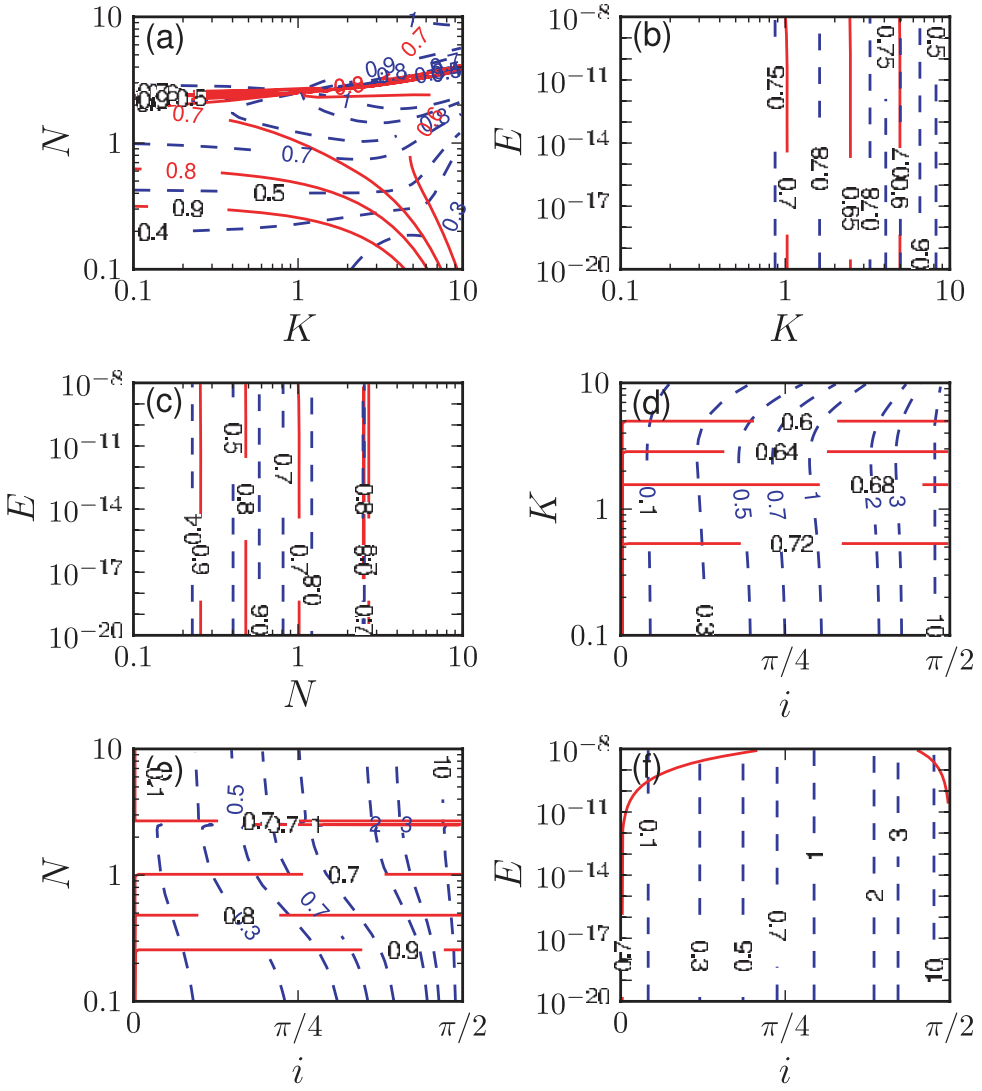

Figure 4. Ratio of fundamental and first-harmonic Fourier amplitudes $|h_+(f_*)|/|h_+(2f_*)|$ (dashed blue contours) and full widths at half-maximum $\Gamma_+(f_*)/\Gamma_+(2f_*)$ (solid red contours) for six slices of the four-dimensional parameter space (N, K, E, i). In each panel, two variables are fixed, with $K = 1$, $N = 1$, $E = 10^{-17}$ and $i = \pi/4$ as appropriate.

be compared to a range of terrestrial experiments and theoretical calculations. The compressibility is commonly expressed in terms of the compression modulus κ, which is related to our normalized compressibility through $K = Am_p gR/\kappa$, where A is the mean atomic number and m_p the proton mass (van Eysden & Melatos 2008). Heavy-ion collisions and nuclear resonance experiments measure κ (Sturm et al. 2001; Vretenar et al. 2003; Piekarewicz 2004; Hartnack et al. 2006). Compressibility can also be inferred from the symmetry energy measured in heavy-ion collisions or obtained through neutron-skin thickness measurements (Chen, Ko & Li 2005; Li, Chen & Ko 2008; Xu et al. 2009). The shear viscosity is often expressed in terms of the ratio η/s, where s is the specific entropy. It is related to the Ekman number by $E = (A'k_B/m_p R^2\Omega)(\eta/s)$ where $1 \leq A' \leq 2$ is the entropy per nucleon in units of Boltzmann's constant (van Eysden & Melatos 2008). The shear viscosity has also been measured in heavy-ion collisions (Adler et al. 2003; Adare et al. 2007). Neutron stars are stably stratified because the concentration of charged particles increases with density but chemical equilibrium is maintained (Reisenegger & Goldreich 1992). Stratification provides a buoyancy force proportional to the Brunt–Väisälä frequency squared, which has been calculated theoretically (Reisenegger & Goldreich 1992; Lai 1994; Passamonti et al. 2009).

In Table 1 we quote a selection of experimental and theoretical values for K, N and E under neutron star conditions. Dimensionless values of N and E assume $\Omega/2\pi = 100$ Hz. In line 1, the compression modulus is inferred from the ratio of the K^+ multiplicity in Au+Au and C+C collisions at $\sim$ GeV energies (Sturm et al. 2001; Hartnack et al. 2006). In line 2, the compression modulus is obtained by fitting a relativistic mean-field model to the distribution of isoscalar monopole and isovector dipole strengths of Zr and Pb (Vretenar et al. 2003; Piekarewicz 2004). In line 3, the compression modulus is obtained from the measured nuclear symmetry energy from isospin diffusion in heavy-ion collisions (Chen et al. 2005; Li et al. 2008). Line 4 lists the ratio of shear viscosity to specific entropy measured in Au+Au collisions at an energy of 200 GeV (Adler et al. 2003; Adare et al. 2007). Theoretical calculations of shear viscosity by Cutler & Lindblom (1987) for neutron–neutron and electron–electron scattering, corresponding to the normal and superfluid states, respectively, are listed in lines 5 and 6. More exotic states, which may exist in the neutron star core, will have a

Downloaded from https://academic.oup.com/mnras/article/409/4/1705/986372 by guest on 16 August 2022

Table 1. Experimental and theoretical results for compressibility, viscosity and Brunt–Väisälä frequency.

Quantity	Experiment/Theory (E/T)	Result	Dimensionless	Reference
K	Au+Au and C+C collisions ($\sim$ GeV) (E)	$\kappa \approx 200$ MeV	$K = 0.97$	1, 2
	Nuclear resonances (E)	$\kappa \approx 240$–270 MeV	$K = 0.72 - 0.81$	3, 4
	Nuclear symmetry energy (E)	$\kappa = 210$ MeV	$K = 0.93$	5, 6
E	Au+Au collisions (200 GeV) (E)	$\eta/s \approx \hbar/4\pi k_B$	$E = 8 \times 10^{-20}$	7, 8
	Neutron–neutron scattering (T)	$\eta = 2 \times 10^{20}$ g cm^{-1} s^{-1}	$E = 5 \times 10^{-9}$	9
	Electron–electron scattering (T)	$\eta = 6 \times 10^{20}$ g cm^{-1} s^{-1}	$E = 1 \times 10^{-8}$	9
	Quark–quark scattering (T)	$\eta = 5 \times 10^{15}$ g cm^{-1} s^{-1}	$E = 1 \times 10^{-13}$	10
N	Chemical composition (T)	$N_* \sim 500$ s^{-1}	$N = 0.8$	11, 12
	Centrifugal correction (T)	$N = 0.32 - 0.84$	$N = 0.32 - 0.84$	13

1, Sturm et al. (2001); 2, Hartnack et al. (2006); 3, Vretenar et al. (2003); 4, Piekarewicz (2004); 5, Chen et al. (2005); 6, Li et al. (2008); 7, Adler et al. (2003); 8, Adare et al. (2007); 9, Cutler & Lindblom (1987); 10, Jaikumar et al. (2008); 11, Reisenegger & Goldreich (1992); 12, Lai (1994); 13, Passamonti et al. (2009).

different viscosity. Line 7 lists the shear viscosity due to quark–quark scattering (Jaikumar, Rupak & Steiner 2008). In lines 8 and 9, we quote calculated values for the Brunt–Väisälä frequency, the latter including centrifugal forces in a rapidly rotating star (Reisenegger & Goldreich 1992; Lai 1994; Passamonti et al. 2009).

6 CONCLUSIONS

In this paper, we calculate analytically the gravitational radiation emitted during the post-glitch recovery phase by the non-axisymmetric Ekman flow excited by a glitch. The calculation is done in the context of an idealized, cylindrical star with a uniform viscosity, compressibility and stratification length-scale. We compute the signal-to-noise ratio for current- and next-generation long-baseline interferometers and find the following promising result: for a large glitch ($\delta\Omega/\Omega = 10^{-4}$) from a neutron star $D = 1$ kpc from Earth and spinning at $f_* = 100$ Hz, the angle-averaged signal-to-noise ratio $\langle d \rangle$ exceeds 3 for $N \lesssim 0.5$, $K \lesssim 10$ and $E \sim 10^{-17}$ with Advanced LIGO and $N \lesssim 1$, $K \lesssim 10$ and $E \sim 10^{-17}$ with ET.

Perhaps the most obvious shortcoming of our idealized model is its cylindrical geometry. There is a noble history of using a cylinder to model spherical astronomical objects and also in classical geophysical studies of the Earth (Pedlosky 1967; Walin 1969; Abney & Epstein 1996; van Eysden & Melatos 2008), because it admits analytic solutions, which in general have not yet been found for a sphere. We ignore magnetic fields for simplicity, although they are large in neutron stars (Cutler 2002), interact with the superfluid (Mendell 1998), and therefore modify Ekman pumping. We model the interior of a neutron star as a single Navier–Stokes fluid, whereas in reality it is a multicomponent superfluid, consisting of superfluid neutrons and superconducting protons which interact with each other via mutual friction and entrainment (e.g. Lattimer & Prakash 2004; Andersson & Comer 2006). The spin-up process in a coupled multicomponent fluid of this kind, in the presence of gravitational stratification and compressibility, is an unsolved and difficult problem.

In our model, the crust accelerates instantaneously from Ω to $\Omega + \delta\Omega$ and remains at this higher angular velocity. A more realistic model would conserve total angular momentum by solving self-consistently for the response of the crust to the viscous back-reaction torque (van Eysden & Melatos 2010). In the context of the present model, we can approximate this effect crudely by replacing the glitch size $\delta\Omega/\Omega$ at $t = 0$ with the permanent frequency jump after the recovery ceases. None of the conclusions change qualitatively.

Understanding the glitch mechanism remains an unsolved problem. Glitch waiting times are exponentially distributed and their sizes fit a power law (Melatos et al. 2008), indicative of inhomogeneous collective behaviour on large scales, e.g. vortex avalanches. In contrast, nuclear structure calculations suggest that the area density of pinning sites (e.g. lattice defects) is much greater than the area density of vortices (Jones 2002; Donati & Pizzochero 2003), suggesting that the system is homogeneous on large scales (pinned Abrikosov array). The gravitational wave signal calculated here helps to discriminate between these two views, as it is a measure of the internal non-axisymmetry. From a simple, random walk argument, the largest relative glitch size that arises from vortex movement in a star containing n vortices is $\delta\Omega/\Omega \sim n^{-1/2}$. If the value of $\delta\Omega/\Omega$ inferred from a gravitational wave detection approaches this maximum, it is safe to infer that large-scale inhomogeneities are present. Note that we take $C_m = 1$ in Section 2.6. However, if only a fraction of the internal flow is non-axisymmetric, C_m should be reduced in proportion. In vortex unpinning models $\delta\Omega/\Omega$ can be up to 4 orders of magnitude larger than the observed glitch size (see Section 4.2), leaving considerable scope to get detectable gravitational wave signals.

Vortex unpinning theories of glitches rely on the build-up of a lag between the crust, which spins down electromagnetically, and the superfluid, whose rotation is fixed by the number of vortices, until a glitch is triggered. We know that the lag does not disappear completely after the glitch (i.e. corotation is not restored) because a reservoir effect (i.e. glitch size $\propto$ waiting time) is not observed in glitch data (Wong, Backer & Lyne 2001); only a small, random fraction of the lag relaxes during a single event, and that fraction is determined by the microscopic history of the system, as in any avalanche process. In this model, we assume conservatively that the crust and fluid co-rotate before the glitch. However, in the more realistic scenario just described, there is ongoing differential rotation between crust and core, suggesting that glitching pulsars may continuously emit gravitational radiation.

Another possibility leading to a continuous gravitational wave signal beyond just the post-glitch recovery period is the 'fossil flow' discussed in Section 3. Stratification prevents Ekman pumping from spinning up the whole interior, leaving a remnant of the initial non-axisymmetric flow untouched. This flow emits gravitational radiation until damped over the much longer diffusion time-scale. If so, we may be able to extend the coherent integration time beyond

Downloaded from https://academic.oup.com/mnras/article/409/4/1705/986372 by guest on 16 August 2022

the recovery time-scale, increasing the likelihood of detection. Even more intriguing is the possibility that any neutron star which has experienced differential rotation in its past retains some part of this fossil flow for $\gtrsim 10^3$ yr, thereby bearing an imprint of the star's formation and rotation history. We plan to study the matter fully in a following paper.

For a typical neutron star at a distance of 1 kpc, the signal-to-noise calculations in Section 4 argue that there is a reasonable chance that interferometers like Advanced LIGO or ET will detect the largest glitches. The outlook is more optimistic if we consider nearby 'dark' neutron stars. For the estimated galactic population of $\sim 10^9$ neutron stars (cf., $\sim$1800 radio pulsars discovered to date), recent Monte Carlo simulations predict that the closest objects are located $\sim$8 pc from the Earth (Ofek 2009). At this distance, Initial LIGO is able to detect the largest glitches with $\langle d \rangle \gtrsim 3$ for $N \lesssim 1$ and $K \lesssim 10$ and Advanced LIGO is sensitive to smaller glitches with $\delta\Omega/\Omega \gtrsim 10^{-6}$. However, the signal frequency, glitch epoch and sky position are unknown electromagnetically, so searching for 'dark' glitches is a difficult proposition. None the less, our results suggest cautious optimism about the chances of detecting a glitching (or otherwise differentially rotating) neutron star with the next generation of gravitational wave interferometers.

ACKNOWLEDGMENTS

We thank the anonymous referee for their helpful comments and suggestions. MFB and CAVE acknowledge the support of Australian Postgraduate Awards.

REFERENCES

Abbott B. et al., 2007a, Phys. Rev. D, 76, 042001
Abbott B. et al., 2007b, Phys. Rev. D, 76, 082001
Abbott B. et al., 2008, ApJ, 683, L45
Abney M., Epstein R. I., 1996, J. Fluid Mech., 312, 327
Adare A. et al., 2007, Phys. Rev. Lett., 98, 172301
Adler S. S. et al., 2003, Phys. Rev. Lett., 91, 182301
Alpar M. A., Nandkumar R., Pines D., 1986, ApJ, 311, 197
Anderson P. W., Itoh N., 1975, Nat, 256, 25
Andersson N., Comer G. L., 2006, Classical Quantum Gravity, 23, 5505
Andersson N., Comer G. L., Glampedakis K., 2005, Nucl. Phys. A, 763, 212
Bai X., Spitkovsky A., 2010, ApJ, 715, 1282
Benton E. R., Clark A., 1974, Ann. Rev. Fluid Mech., 6, 257
Bonazzola S., Gourgoulhon E., 1996, A&A, 312, 675
Bondarescu R., Teukolsky S. A., Wasserman I., 2007, Phys. Rev. D, 76, 064019
Brink J., Teukolsky S. A., Wasserman I., 2004, Phys. Rev. D, 70, 124017
Chen L., Ko C. M., Li B., 2005, Phys. Rev. Lett., 94, 032701
Clark J., Heng I. S., Pitkin M., Woan G., 2007, Phys. Rev. D, 76, 043003
Cutler C., 2002, Phys. Rev. D, 66, 084025
Cutler C., Lindblom L., 1987, ApJ, 314, 234
Dodson R. G., McCulloch P. M., Lewis D. R., 2002, ApJ, 564, L85
Donati P., Pizzochero P. M., 2003, Phys. Rev. Lett., 90, 211101
Easson I., 1979, ApJ, 228, 257
Greenspan H. P., Howard L. N., 1963, J. Fluid Mech., 17, 385
Hartnack C., Oeschler H., Aichelin J., 2006, J. Phys. G Nucl. Phys., 32, 231
Haskell B., Jones D. I., Andersson N., 2006, MNRAS, 373, 1423
Hayama K., Desai S., Mohanty S. D., Rakhmanov M., Summerscales T., Yoshida S., 2008, Classical Quantum Gravity, 25, 184016
Hibschman J. A., Arons J., 2001, ApJ, 546, 382
Hild S., Chelkowski S., Freise A., 2008, preprint (arXiv:0810.0604)
Hild S., Chelkowski S., Freise A., Franc J., Morgado N., Flaminio R., DeSalvo R., 2010, Classical Quantum Gravity, 27, 015003
Jaikumar P., Rupak G., Steiner A. W., 2008, Phys. Rev. D, 78, 123007
Jaranowski P., Królak A., Schutz B. F., 1998, Phys. Rev. D, 58, 063001
Jensen H. J., 1998, Self-Organized Criticality: Emergent Complex Behavior in Physical and Biological Systems. Cambridge Univ. Press, Cambridge
Jones D. I., Andersson N., 2002, MNRAS, 331, 203
Jones P. B., 2002, MNRAS, 335, 733
Junk M., Egbers C., 2000, in Egbers C., Pfister G., eds, Lecture Notes Phys. Vol. 549, Physics of Rotating Fluids. Springer-Verlag, Berlin, p. 215
Lai D., 1994, MNRAS, 270, 611
Lattimer J. M., Prakash M., 2004, Sci, 304, 536
Lattimer J. M., Prakash M., 2007, Phys. Rep., 442, 109
Li B., Chen L., Ko C. M., 2008, Phys. Rep., 464, 113
Lyne A. G., Manchester R. N., 1988, MNRAS, 234, 477
McCulloch P. M., Hamilton P. A., McConnell D., King E. A., 1990, Nat, 346, 822
Melatos A., Payne D. J. B., 2005, ApJ, 623, 1044
Melatos A., Peralta C., 2007, ApJ, 662, L99
Melatos A., Peralta C., 2010, ApJ, 709, 77
Melatos A., Warszawski L., 2009, ApJ, 700, 1524
Melatos A., Peralta C., Wyithe J. S. B., 2008, ApJ, 672, 1103
Mendell G., 1998, MNRAS, 296, 903
Munson B. R., Menguturk M., 1975, J. Fluid Mech., 69, 705
Nakabayashi K., 1983, J. Fluid Mech., 132, 209
Nayyar M., Owen B. J., 2006, Phys. Rev. D, 73, 084001
Ofek E. O., 2009, PASP, 121, 814
Owen B. J., Reitze D. H., Whitcomb S. E., 2009, preprint (arXiv:0903.2603)
Passamonti A., Haskell B., Andersson N., Jones D. I., Hawke I., 2009, MNRAS, 394, 730
Payne D. J. B., Melatos A., 2006, ApJ, 641, 471
Pedlosky J., 1967, J. Fluid Mech., 28, 463
Peralta C., Melatos A., 2009, ApJ, 701, L75
Peralta C., Melatos A., Giacobello M., Ooi A., 2005, ApJ, 635, 1224
Peralta C., Melatos A., Giacobello M., Ooi A., 2006a, ApJ, 644, L53
Peralta C., Melatos A., Giacobello M., Ooi A., 2006b, ApJ, 651, 1079
Peralta C., Melatos A., Giacobello M., Ooi A., 2008, J. Fluid Mech., 609, 221
Peralta C. A., 2006, PhD thesis, Univ. Melbourne, Australia
Piekarewicz J., 2004, Phys. Rev. C, 69, 041301
Reisenegger A., Goldreich P., 1992, ApJ, 395, 240
Sedrakian D. M., Benacquista M., Shahabassian K. M., Sadoyan A. A., Hairapetyan M. V., 2003, Astrophys., 46, 445
Shemar S. L., Lyne A. G., 1996, MNRAS, 282, 677
Sidery T., Passamonti A., Andersson N., 2010, MNRAS, 405, 1061
Sturm C. et al., 2001, Phys. Rev. Lett., 86, 39
Thorne K. S., 1980, Rev. Modern Phys., 52, 299
Ushomirsky G., Cutler C., Bildsten L., 2000, MNRAS, 319, 902
van Eysden C. A., Melatos A., 2008, Classical Quantum Gravity, 25, 225020
van Eysden C. A., Melatos A., 2010, MNRAS, submitted
Vigelius M., Melatos A., 2009, MNRAS, 395, 1972
Vretenar D., Nikšić T., Ring P., 2003, Phys. Rev. C, 68, 024310
Walin G., 1969, J. Fluid Mech., 36, 289
Warszawski L., Melatos A., 2008, MNRAS, 390, 175
Wong T., Backer D. C., Lyne A. G., 2001, ApJ, 548, 447
Xu J., Chen L., Li B., Ma H., 2009, Phys. Rev. C, 79, 035802

APPENDIX A: SIMPLIFYING $\boldsymbol{x} \cdot \mathbf{curl}(\rho \boldsymbol{v})$

It is straightforward to evaluate S^{lm} by substituting (23)–(27) directly into (34). However, the calculation is easier and more transparent if we first simplify the integrand in (34) to depend only on δp. Expanding according to $\rho \mapsto \rho^0 + \delta\rho$, $\boldsymbol{v} \mapsto \boldsymbol{v}^0 + \boldsymbol{\delta v} = r\Omega \boldsymbol{e}_\phi + \boldsymbol{\delta v}$, we express the integrand to first order as

$$\boldsymbol{x} \cdot \nabla \times (\rho^0 \boldsymbol{v}^0 + \delta\rho \boldsymbol{v}^0 + \rho^0 \boldsymbol{\delta v}). \tag{A1}$$

Downloaded from https://academic.oup.com/mnras/article/409/4/1705/986372 by guest on 16 August 2022

The first term in (A1) is independent of time. It does not emit gravitational radiation, so we discard it. The second term in (A1) reads

$$\boldsymbol{x}\cdot\nabla\times(\delta\rho\boldsymbol{v}^0)=\Omega\left(2z+rz\frac{\partial}{\partial r}-r^2\frac{\partial}{\partial z}\right)\delta\rho \tag{A2}$$

$$=\frac{\Omega}{g}\left(r^2\frac{\partial^2}{\partial z^2}-rz\frac{\partial^2}{\partial r\partial z}-2z\frac{\partial}{\partial z}\right)\delta p. \tag{A3}$$

To move from (A2) to (A3) we use the Navier–Stokes equation (1) to first order in Rossby number and zeroth order in Ekman number. In the rotating frame and neglecting the centrifugal term, as in Section 2, it reads

$$2\rho^0(\boldsymbol{\Omega}\times\boldsymbol{\delta v})=-\nabla\delta p-\boldsymbol{g}\delta\rho, \tag{A4}$$

from which we obtain

$$\delta\rho=-\frac{1}{g}\frac{\partial\delta p}{\partial z}. \tag{A5}$$

The third term in (A1) can be rewritten in a similar way. From (A4), we find

$$2\Omega\rho^0\boldsymbol{e}_z\times(\boldsymbol{e}_z\times\boldsymbol{\delta v})=\nabla\times(\delta p\boldsymbol{e}_z), \tag{A6}$$

where ($\boldsymbol{e_r}$, $\boldsymbol{e}_\phi$, $\boldsymbol{e}_z$) are the basis vectors in cylindrical coordinates. Noting that $\delta v_z^0=0$, as the axial flow is $O(E^{1/2})$, we are left with

$$\rho^0\boldsymbol{\delta v}=-\frac{1}{2\Omega}\nabla\times(\delta p\boldsymbol{e}_z), \tag{A7}$$

and the third term in (A1) is

$$\boldsymbol{x}\cdot\nabla\times(\rho^0\boldsymbol{\delta v})=\frac{1}{2\Omega}\left(z\nabla^2-r\frac{\partial^2}{\partial r\partial z}-z\frac{\partial^2}{\partial z^2}\right)\delta p. \tag{A8}$$

Combining (A3) and (A8), and replacing $\partial^2/\partial\phi^2$ by $-m^2$, we arrive at

$$\boldsymbol{x}\cdot\nabla\times(\rho\boldsymbol{v})=\left[\frac{1}{2\Omega}\left(z\frac{\partial^2}{\partial r^2}+\frac{z}{r}\frac{\partial}{\partial r}-\frac{zm^2}{r^2}-r\frac{\partial^2}{\partial r\partial z}\right)+\frac{\Omega}{g}\left(r^2\frac{\partial^2}{\partial z^2}-rz\frac{\partial^2}{\partial r\partial z}-2z\frac{\partial}{\partial z}\right)\right]\delta p^0. \tag{A9}$$

There is a subtle issue around neglecting the centrifugal correction to (A4), which is of order F. If we evaluate S^{lm} by substituting (23)–(27) directly into (34), we implicitly include centrifugal terms in $\boldsymbol{x}\cdot\nabla\times(\rho\boldsymbol{v})$ (by virtue of failing to exclude them explicitly). This approach is internally inconsistent, because centrifugal terms of this order are excluded from the flow fields (23)–(27) following the assumption in Section 2.2 leading to (5) and (6). It is therefore preferable to evaluate (34) for S^{lm} using (A9), so that the centrifugal correction to the zeroth-order structure is consistently excluded from both the flow fields and S^{lm}.

APPENDIX B: BEAM PATTERN FUNCTIONS

The complete expressions for the beam pattern functions are (Jaranowski et al. 1998)

$$F_+(t)=\sin\zeta[a(t)\cos2\psi+b(t)\sin2\psi], \tag{B1}$$

$$F_\times(t)=\sin\zeta[b(t)\cos2\psi-a(t)\sin2\psi], \tag{B2}$$

with

$$\begin{aligned}a(t)=&\frac{1}{16}\sin2\gamma(3-\cos2\lambda)(3-\cos2\delta)\cos[2(\alpha-\phi_r-\Omega_rt)]\\&-\frac{1}{4}\cos2\gamma\sin\lambda(3-\cos2\delta)\sin[2(\alpha-\phi_r-\Omega_rt)]\\&+\frac{1}{4}\sin2\gamma\sin2\lambda\sin2\delta\cos[\alpha-\phi_r-\Omega_rt]\\&-\frac{1}{2}\cos2\gamma\cos\lambda\sin2\delta\sin[\alpha-\phi_r-\Omega_rt]\\&+\frac{3}{4}\sin2\gamma\cos^2\lambda\cos^2\delta,\end{aligned} \tag{B3}$$

$$\begin{aligned}b(t)=&\cos2\gamma\sin\lambda\sin\delta\cos[2(\alpha-\phi_r-\Omega_rt)]\\&+\frac{1}{4}\sin2\gamma(3-\cos2\lambda)\sin\delta\sin[2(\alpha-\phi_r-\Omega_rt)]\\&+\cos2\gamma\cos\lambda\cos\delta\cos[\alpha-\phi_r-\Omega_rt]\\&+\frac{1}{2}\sin2\gamma\sin2\lambda\cos\delta\sin[\alpha-\phi_r-\Omega_rt].\end{aligned} \tag{B4}$$

The right ascension and declination of the gravitational wave source are given by α and δ, respectively, and ψ is the polarization angle. The latitude of the detector is denoted by λ, Ω_r is the angular velocity of the Earth and ϕ_r is the diurnal phase of the Earth. The angle counterclockwise between east and the bisector of the interferometer arms is γ, and the angle between the arms of the interferometer is ζ. We average over α, δ and ψ according to Jaranowski et al. (1998)

$$\langle\ldots\rangle_{\alpha,\delta,\psi}=\frac{1}{2\pi}\int_0^{2\pi}\mathrm{d}\alpha\times\frac{1}{2}\int_{-1}^{1}\mathrm{d}(\sin\delta)\times\frac{1}{2\pi}\int_0^{2\pi}\mathrm{d}\psi\,(\ldots). \tag{B5}$$

We evaluate $\langle\int_0^{T_0}\mathrm{d}t\,F_+^2\rangle_{\alpha,\delta,\psi}$ and $\langle\int_0^{T_0}\mathrm{d}t\,F_\times^2\rangle_{\alpha,\delta,\psi}$ for use in Section 4. Averaging (B1) and (B2) over ψ, we obtain

$$\begin{aligned}\left\langle\int_0^{T_0}\mathrm{d}t\,F_+^2\right\rangle_\psi&=\left\langle\int_0^{T_0}\mathrm{d}t\,F_\times^2\right\rangle_\psi\\&=\frac{1}{2}\sin^2\zeta\int_0^{T_0}\mathrm{d}t\left([a(t)]^2+[b(t)]^2\right).\end{aligned} \tag{B6}$$

All the dependence on α and δ is contained in $a(t)$ and $b(t)$. After some straightforward but lengthy algebra, we find that the dependence on all other angles drops out, leaving

$$\left\langle[a(t)]^2+[b(t)]^2\right\rangle_{\alpha,\delta}=\frac{2}{5}. \tag{B7}$$

Substituting (B7) into (B6) and evaluating the now-trivial time integration, we obtain the result stated in equation (53):

$$\left\langle\int_0^{T_0}\mathrm{d}t\,F_+^2\right\rangle_{\alpha,\delta,\psi}=\left\langle\int_0^{T_0}\mathrm{d}t\,F_\times^2\right\rangle_{\alpha,\delta,\psi}=\frac{T_0}{5}\sin^2\zeta. \tag{B8}$$

This paper has been typeset from a TEX/LATEX file prepared by the author.

Downloaded from https://academic.oup.com/mnras/article/409/4/1705/986372 by guest on 16 August 2022